

The formation of NGC 3603 young starburst cluster: “prompt” hierarchical assembly or monolithic starburst?

Sambaran Banerjee^{1*} and Pavel Kroupa¹

¹*University of Bonn, Auf dem Hügel 71, D-53121, Bonn, Germany*

Submitted August, 2014

ABSTRACT

The formation of very young massive clusters or “starburst” clusters is currently one of the most widely debated topic in astronomy. The classical notion dictates that a star cluster is formed in-situ in a dense molecular gas clump. The stellar radiative and mechanical feedback to the residual gas energizes the latter until it escapes the system. The newly born gas-free young cluster eventually readjusts with the corresponding mass loss. Based on the observed substructured morphologies of many young stellar associations, it is alternatively suggested that even the smooth-profiled massive clusters are also assembled from migrating less massive subclusters. A very young (age ≈ 1 Myr), massive ($> 10^4 M_{\odot}$) star cluster like the Galactic NGC 3603 young cluster (HD 97950) is an appropriate testbed for distinguishing between the above “monolithic” and “hierarchical” formation scenarios. A recent study by Banerjee and Kroupa (2014) demonstrates that the monolithic scenario remarkably reproduces the HD 97950 cluster. In particular, its shape, internal motion and the mass distribution of stars are found to follow naturally and consistently from a single model calculation undergoing $\approx 70\%$ by mass gas dispersal. In the present work, we explore the possibility of the formation of the above cluster via hierarchical assembly of subclusters. These subclusters are initially distributed over a wide range of spatial volumes and have various modes of sub-clustering in both absence and presence of a background gas potential. Unlike the above monolithic initial system that reproduces HD 97950 very well, the same is found to be prohibitive with hierarchical assembly alone (with/without a gas potential). Only those systems which assemble promptly into a single cluster (in $\lesssim 1$ Myr) from a close separation (all within $\lesssim 2$ pc) could match the observed density profile of HD 97950 after a similar gas removal. These results therefore suggest that the NGC 3603 young cluster has formed essentially monolithically, *i.e.*, either in-situ or via a prompt assembly, followed by a substantial residual gas expulsion. Both scenarios are consistent with the inferred young age and the small age spread of this cluster. Future observations of molecular cloud filaments with *ALMA* and proper motion measurements of young clusters with *Gaia* will provide more direct tests of such birth environments.

Key words: stars: kinematics and dynamics – methods: numerical – open clusters and associations: individual(NGC 3603 young cluster) – galaxies: star formation – galaxies: starburst – galaxies: star clusters: general

1 INTRODUCTION

How very young (age of a few Myr), massive (rich) star clusters (hereafter VYMCs as coined by Banerjee & Kroupa 2014; also known as “starburst” clusters) of near-spherical shape form out of vast molecular clouds is one of the most debated topic in astrophysics. The most massive ones are typically found in an overall near-spherical core-halo form

and they can be surrounded by a cocoon of HII (ionized hydrogen) region. Perhaps the most widely discussed among such systems are the R136 cluster in the Large Magellanic Cloud (LMC), the central cluster (HD 97950; hereafter HD97950) of the Galactic “Giant Nebula” NGC 3603 and the Arches cluster (Portegies Zwart et al. 2010). Several VYMCs are found as the richest member of extended cluster complexes/stellar associations, *e.g.*, the ONC (Alves & Bouy 2012). Young stellar systems are also found as extended associations of OB stars, *e.g.*, the Cygnus OB2 (Kuhn et al.

* Corresponding author. E-mail: sambaran@astro.uni-bonn.de

2014; Wright et al. 2014). The highly compact young cluster RCW 38 is a special case which is mostly embedded in molecular hydrogen except its central region (DeRose et al. 2009). In several cases there are indications that even an overall core-halo shaped VYMC also contains substructures, as obtained from the “Massive Young Star-Forming Complex Study in Infrared and X-ray” (MYStIX; Feigelson et al. 2013) survey catalog (Kuhn et al. 2014).

At present, there exist apparently at least two distinct scenarios for formation of VYMCs. The monolithic or episodic (top-down) scenario dictates the formation of a compact star cluster in an essentially single but highly active star-formation episode. The infant cluster of pre-main-sequence (PMS) and main sequence (MS) stars remains embedded in its parent molecular gas cloud where the latter gets energized (and ionized) by the radiation and material outflows from the stars. Such energy injection eventually causes the embedding gas to become gravitationally unbound from the system and disperse in a timescale typically comparable to the dynamical time of the stellar system, *i.e.*, too fast for the stars to adjust with the corresponding reduction of potential well. This causes the gas-free stellar system to expand violently and lose a fraction of its stars depending on its initial mass and concentration (Adams 2000; Kroupa et al. 2001; Baumgardt & Kroupa 2007; Banerjee & Kroupa 2013; Pfalzner & Kaczmarek 2013). The remaining system may eventually regain virial or dynamical equilibrium (re-virialization); hence a particular VYMC may or may not be in dynamical equilibrium depending on the time taken to re-virialize and the epoch at which it is observed (Banerjee & Kroupa 2013). Such a “monolithic” or top-down scenario has successfully explained well observed VYMCs, *e.g.*, ONC (also the Pleiades; Kroupa et al. 2001), R136 (Banerjee & Kroupa 2013) and the NGC 3603 young cluster (Banerjee & Kroupa 2014).

Alternatively, VYMCs are thought to have formed “bottom-up” via merging of less massive subclusters (Longmore et al. 2014). These subclusters are usually thought to form with high local star formation efficiency (SFE), *i.e.*, they convert a large fraction of the gas in their vicinity into stars. Several of such subclusters fall onto each other and merge to form the final VYMC. The gravitational potential of the background molecular gas within which these subclusters appear augments the infall rate (the so-called “conveyor belt mechanism”; Longmore et al. 2014). The observational motivation for such a scenario is the apparent substructures in OB associations and even in VYMCs having overall core-halo configurations (Kuhn et al. 2014). On the theoretical side, star formation has been investigated in hydrodynamic calculations involving development of seed turbulence, in cubical/spherical gas clouds, into high-density filaments where star (sink particle) formation occurs as a result of gravitational collapse and fragmentation (Klessen et al. 1998; Bate & Bonnell 2004; Girichidis et al. 2011).

In such calculations, small clusters of proto-stars are formed in filaments and/or filament nodes over a short period of time, which then fall collectively into the potential of the cloud to form larger (gas-embedded) clusters (*e.g.*, in Bate 2009 and Girichidis et al. 2011). Different groups have reached the state-of-the-art of such calculations by incorporating physical processes in different degrees of detail but for mass scales much lighter than VYMCs. Such smoothed-

particle-hydrodynamic (SPH) self-star-forming calculations, requiring very high particle resolution, is formidable for the mass range of VYMCs ($> 10^4 M_\odot$). High-resolution (reaching the “opacity limit”) SPH computations have so far been done forming stars in spherical gas clouds of up to $\approx 500 M_\odot$ only (Klessen et al. 1998; Bate & Bonnell 2004; Bate 2009; Girichidis et al. 2011, 2012; Bate 2012) but without any feedback and hence self-regulation mechanism. Radiation-magnetohydrodynamic (MHD) calculations including stellar feedback (radiation and matter outflows) to the star-forming gas have also been carried out from proto-stellar scales (Machida & Matsumoto 2012; Bate et al. 2014) up to $\approx 50 M_\odot$ gas spheres (Price & Bate 2010). While the latter studies provide insights into the self-regulation mechanisms in the star formation process and point to an SFE near 30%, consistently with observations (Lada & Lada 2003), the processes that lead to the ultimate dispersal of the residual gas are still unclear (Matthew Bate, University of Exeter, U.K.: private communication). More recently, an independent semi-analytical study (Banerjee 2014) of formation of clump-cores (that would eventually turn into proto-stars) in gas clumps and of the maximum mass of the cores infers an upper limit of $\approx 30\%$ for the clump SFE. This is consistent with the hydrodynamic calculations with self-regulation and observations in the solar neighborhood (see above).

Note that the gas has to disperse from the region in the molecular cloud where the cluster ultimately assembles, to obtain a gas-free young cluster like what we see today. The only way the essential dynamical effects of gas dispersal can be included is to adopt a time-varying background potential mimicking the effect of the gas, which is widely used (Kroupa et al. 2001; Pfalzner & Kaczmarek 2013; Banerjee & Kroupa 2014). The latter approach has successfully explained several well observed VYMCs, *viz.*, the Galactic ONC (Kroupa et al. 2001) and NGC 3603 (Banerjee & Kroupa 2014) and R136 (Banerjee & Kroupa 2013) of the LMC. These studies point to a universal SFE of $\epsilon \approx 33\%$ and a sonic dispersal of the residual ionized hydrogen or HII gas (see Banerjee & Kroupa 2013 and references therein), remarkably reproducing the measured kinematic and structural properties of these clusters. The dynamical process of coalescence of subclusters into more massive clusters has also been studied recently using direct N-body calculations in both absence (Fujii et al. 2012) and presence (Smith et al. 2013) of a background gas potential. The role of this process is also investigated in the context of formation of dwarf galaxies through merger of young massive clusters (Amaro-Seoane et al. 2014).

The work reported in the present paper focuses on formation of VYMCs through subcluster merging. In particular, we consider the reproducibility of the VYMC HD97950 in the Galactic NGC 3603 star forming region from a wide range of initially subclustered conditions. As in Banerjee & Kroupa (2014), we target this cluster again due to the availability of its detailed, high-quality structural and kinematical data from the Very Large Telescope (VLT; Harayama et al. 2008) and the Hubble Space Telescope (HST; Rochau et al. 2010; Pang et al. 2013). Situated on the Carina spiral arm of the Milky way at a distance of $\approx 6 - 7$ kpc from the Sun, HD97950 is our nearest starburst cluster and also perhaps the most well observed one. Furthermore, its large mass (photometrically $10000 M_\odot - 16000 M_\odot$; Stolte et al. 2006;

Harayama et al. 2008), extreme young age of ≈ 1 Myr with a small age spread (Stolte et al. 2004; Pang et al. 2013) despite having a clear core-halo configuration makes HD97950 ideal for testing theories of VYMC/globular cluster formation. Fig. 1 shows an HST image of HD97950. Table 1 summarizes the observed properties of HD97950 which will be referred to in the following sections at different occasions.

We explore a wide range of initial subclustering mode and the spatial volume over which the subclusters are distributed. We also explore the effects of the presence of a background gas potential. We demonstrate that prompt merging of subclusters that fall onto each other from close initial separations ($\lesssim 1$ pc) followed by a substantial gas expulsion ($\approx 70\%$ by mass) can reproduce the observed surface density profile of the HD97950 cluster. These calculations also suggest that a significant amount of gas expulsion is essential for getting the observed profile right. Nevertheless, the overall agreement with both the structural and kinematic data of the cluster is better achieved with the monolithic model of Banerjee & Kroupa (2014) than the hierarchical formation models as computed here.

2 INITIAL CONDITIONS

In the following sections we detail our calculations that aim to form the observed HD97950 cluster through subcluster merging, starting from a range of initial configurations. We also discriminate the cases where the subclusters fall in under the influence of a background gas potential and those where the infall occurs only under the mutual gravity of the subclusters. The objective is to determine the timescales for formation of core-halo configurations beginning from various substructured initial conditions vis-a-vis the present age of HD97950. We also determine the conditions under which the final core-halo cluster agrees with the observed profile and kinematics of HD97950.

2.1 Initial (proto) stellar distribution

The substructured initial conditions are generated by distributing compact Plummer spheres (Plummer 1911) uniformly over a spherical volume of radius R_0 . The total stellar mass distributed in this way is always the lower photometric mass estimate of $M_* \approx 10^4 M_\odot$ for HD97950. One motivation for adopting the lower mass limit is the study of Banerjee & Kroupa (2014) where a monolithic embedded cluster of the above total stellar mass turns out to be optimal in reproducing the HD97950 cluster after gas expulsion. As we will see below, this is true in this case also.

The above fashion of initial subclustering is an idealization and extrapolation of what is found in the largest SPH calculations of cluster formation to date (Bate 2009, 2012; Girichidis et al. 2011). In these calculations, the uniformly dense and turbulent gas spheres develop multiple high-density filamentary structures (as what is observed in molecular clouds) where typically 1-2 subclusters appear per filament at their densest points and also at the filament junctions. This is consistent with what is observed in dense molecular gas filaments, *e.g.*, through the *Herschel* telescope (Schneider et al. 2010, 2012). These filaments often extend

across the spherical cloud and can have arbitrarily bent configuration so that subclusters can appear anywhere within the sphere. Also, most of the filaments and the subclusters are found to form promptly. Hence, although the total gas mass used in these SPH calculations are about an order of magnitude smaller than the above M_* and the total mass of proto-stars formed is up to 20% of the gas mass (Girichidis et al. 2011), the above mode of subclustering is an idealized but appropriate extension of the state-of-the-art hydrodynamic calculations.

The Plummer shape of the subclusters also conform with the observed Plummer profile of the filament sections in molecular clouds (Malinen et al. 2012). We choose the half-mass radii, $r_h(0)$, of these Plummer spheres to be typically between 0.1–0.3 pc, in accordance with the observed widths of these highly compact molecular-cloud filaments (André et al. 2011; Schneider et al. 2012). Such compact sizes of the subclusters are also consistent with those observed in stellar complexes, *e.g.*, the Taurus-Auriga stellar groups (Palla & Stahler 2002; Kroupa & Bouvier 2003). However, in some calculations, we also use larger $r_h(0)$ (see below).

The number of subclusters, n , over which the $M_* \approx 10^4 M_\odot$ is subdivided has to be chosen somewhat arbitrarily (as in recent studies, *e.g.*, Fujii et al. 2012). In the above mentioned hydrodynamic calculations, subclusters containing 10s to 100s of proto-stars (sink particles) could form (subject to the caveat that sink particle formation continues unhindered by stellar feedback). However, it is not straightforward to extrapolate the richness of subclusters to the much larger masses as in here. In order to incorporate a range of possibilities, we consider two primary cases of the initial subdivision of the total stellar mass. The “blobby” (type A) systems consist of 10 subclusters of $m_{cl}(0) \approx 10^3 M_\odot$ each. Panels 1, 2, 4 and 6 of Fig. 2 are examples of such initial systems. Note that in this and all the subsequent figures, the panels are numbered left-to-right, top-to-bottom. On the other hand, “grainy” (type B) systems comprise ≈ 150 subclusters with mass range $10 M_\odot \lesssim m_{cl}(0) \lesssim 100 M_\odot$ summing up to $M_* \approx 10^4 M_\odot$. We show below that the mode of initial subdivision does not influence the primary results.

The initial spanning radius, R_0 , is chosen over a wide range, *viz.*, $0.5 \text{ pc} \lesssim R_0 \lesssim 10.0 \text{ pc}$, to explore the wide range of molecular cloud densities (see below) and spatial extents as observed in star-forming regions and stellar complexes. Tables 3 and 5 (their first and second columns) provide a complete list of the initial conditions for the computations here. The detailed nomenclature, in their first columns, is explained in Table 3 and the corresponding short names, in their second columns, are self-explanatory.

The stellar mass function of the individual subclusters is taken to be canonical (Kroupa 2001; Kroupa et al. 2013) and is drawn from a probability distribution without an upper bound. Note that the stellar entities here are proto-stars which are yet to reach their hydrogen-burning main sequences (a few most massive members can become MS during their infall depending on the infall time). Furthermore, the interplay between gas accretion and dynamical processes (ejections, mergers) during the infall and the final assembly of the main cluster continue to shape the global stellar mass function or the initial mass function (IMF) of the final cluster (Klessen et al. 1998). This IMF is often ob-

served to be canonical for VYMCs. Note that the accretion and the dynamical processes only influence the massive tail of the IMF and also sets the maximum stellar mass (Weidner & Kroupa 2004; Weidner & Pflamm-Altenburg 2013) of the *final* cluster, as indicated in hydrodynamic calculations (Klessen et al. 1998; Girichidis et al. 2011). The overall canonical form of the IMF as determined by the low mass stars, which contribute to most of the stellar mass of a subcluster (> 90%), appears mostly due to gravitational fragmentation alone. This justifies our adopting of the unconditional canonical IMF as a suitable representation of the proto-stellar mass function of the subclusters, despite the exclusion of gas accretion in the calculations here. Again, the proto-stellar mass function does not critically impact the primary results here.

Finally, all subclusters are initially at rest w.r.t. the centre of mass (COM) of the stellar system. While this initial condition is again an idealization, it is consistent with the results of detailed hydrodynamic computations. In these calculations, the newly formed subclusters in the high-density filaments and at the filament junctions typically move with velocities which are much smaller than the average turbulent velocity of the gas cloud and hence form a sub-virial system of subclusters (see, *e.g.*, Bate & Bonnell 2004; Bate 2009). As long as the initial system of clusters is sub-virial, the timescales inferred from the calculations here would not be affected significantly.

Primordial binaries are currently excluded for the ease of computing. The presence of primordial binaries does not affect the subcluster merging process substantially as found in test calculations (see Sec. 3.2).

2.2 Initial gas potential

The dense residual molecular cloud, within which the proto-stars form in distinct subclusters (see Sec. 2.1), is represented by a background, external gravitational potential of a Plummer mass distribution. In this way the overall dynamical effect of the molecular cloud is included. In order to compare with the previous studies (Kroupa et al. 2001; Banerjee & Kroupa 2014), we adopt a local SFE of $\epsilon \approx 1/3$. Such SFE is also consistent with those obtained from hydrodynamic calculations including self-regulation (Machida & Matsumoto 2012; Bate et al. 2014) and as well with observations of embedded systems in the solar neighborhood (Lada & Lada 2003).

Hence, we place the geometric/density centre of the Plummer gas sphere co-incident with the COM of the initial stellar system and take the half-mass radius of the former equal to the initial span R_0 of the subclusters (see Sec. 2.1). To achieve a local (cluster-scale) SFE of $\epsilon \approx 1/3$, the total gas mass within R_0 is taken to be $2M_*$, *i.e.*, the total matter (gas + stars) within the R_0 -sphere is $3M_*$. Since R_0 is equal to the half-mass radius of the Plummer gas sphere, the total mass of the spherical gas cloud is $4M_*$ and, including the stars, the entire system contains $5M_*$ of matter. In principle, star clusters can also appear beyond the half-mass radius of the gas cloud although the probability of forming them within is higher because of the higher average gas density there. Hence, the above initial setup is again an idealization to set the intended SFE. It is also consistent with the uniform initial distribution of the subclusters

within R_0 since the density is nearly uniform within the Plummer half-mass radius. Note that although the SFE is $M_*/3M_* = 33\%$ within R_0 , it is $M_*/5M_* = 20\%$ for entire gas cloud. These numbers are consistent with what is found in the recent hydrodynamic calculations (see Secs. 1 and 2.1) of star formation and are also consistent with observations (Lada & Lada 2003).

Inserting our adopted value $M_* = 10^4 M_\odot$ (see Sec. 2.1), we get a total of $3 \times 10^4 M_\odot$ (gas + stars) within R_0 . This gives an ONC-like $\rho_g \approx 6 \times 10^3 M_\odot \text{pc}^{-3}$ gas density for $R_0 = 1.06 \text{ pc}$ and $\approx 1/1000$ th of this for $R_0 = 10 \text{ pc}$ which is appropriate for, *e.g.*, the Taurus-Auriga complex of subclusters.

The analytic Plummer gas cloud is geometrically static but its total mass is reduced exponentially to mimic gas expulsion as in Kroupa et al. (2001); Banerjee & Kroupa (2013). We use this treatment to be able to compare the present calculations with the previous ones. Dynamical gas expulsion in SPH-based calculations have shown this treatment to yield well comparable results (Geyer & Burkert 2001). Note that the spherically symmetric gas expulsion from beyond R_0 (which has a total mass of $2M_*$) will not influence the stellar system within R_0 since the former fraction of gas imparts zero gravitational force within R_0 . Hence, the expulsion of the entire $4M_*$ Plummer sphere has essentially the same dynamical effect on the stellar system as the expulsion of just the $2M_*$ gas (which is appropriate for $\approx 33\%$ SFE) from within R_0 . We address some additional issues in Sec. 4.

3 DYNAMICAL EVOLUTION OF THE SUBCLUSTER SYSTEMS

The above initial configurations (see Table 3 & 5) are generated using a self-developed automated script. Its final outcome is the combined masses, positions and velocities for all the stars in all subclusters for a particular configuration. The script uses the MCLUSTER code (Küpper et al. 2011) to generate the individual Plummer spheres.

We evolve the above initial configurations using the state-of-the-art direct N-body integrator NBODY6 (Aarseth 2003). The initial configuration data can be directly fed to the NBODY6 code. The spherically symmetric background gas potential (see Sec. 2.2) can also be initiated and varied over time from within the N-body code. NBODY6 is a highly sophisticated N-body integrator which uses a fourth-order Hermite scheme and particle-specific time steps to compute the trajectories of the individual mass points. The diverging gravitational force between two close-passing masses or that between the components of a close binary or a multiplet is handled using two- and few-body regularization (Aarseth 2003).

NBODY6 includes the widely-used semi-analytic binary evolution scheme BSE (Hurley et al. 2000) to evolve the individual stars starting from their main sequence. However, BSE does not include a reliable PMS evolution. Hence, in the NBODY6 calculations here, we do not activate the stellar evolution. However, we do a few test calculations with the main sequence evolution to qualitatively assess any effect of stellar winds. Since we are primarily interested in the configurations at very young ages when the most massive stars

are still on their main sequence, stellar wind mass loss would not severely influence the massive stellar spectrum and the associated dynamical consequences.

3.1 General evolutionary properties

The generic evolution of a given configuration consists of three parts, *viz.*, (a) the net infall of each subcluster towards the global minimum of the gravitational potential well of the system, (b) the two-body relaxation of each subcluster while they fall in and (c) the final coalescence of the subclusters to approach a system in dynamical (virial) equilibrium. The global potential minimum of the system roughly corresponds to the system’s COM. The background Plummer gas potential (see Sec. 2.2), if present, is the dominant component of the global potential well. The infalling subclusters eventually merge and form a (near) spherical core-halo stellar distribution which is in dynamical equilibrium. During the infall and the merger process, the potential well of the system changes with time but the final virialized stellar distribution and the global minimum of the final potential well must be concentric for an energetically stable configuration. The final virialized stellar distribution has also much smaller spatial extent than their initial extent R_0 (see below).

The timescale in which the system arrives at the smooth-profiled, single cluster configuration is primarily determined by the initial span, R_0 , of the subclusters. R_0 determines the time taken for the subclusters to cross their orbital pericenters (or fall through the potential minimum for strictly radial orbits). The background gas potential, of course, accelerates the initial infall. Starting from rest, as in the present case (see Sec. 2.1), the subclusters’ pericenters are typically close to the potential minimum, *i.e.*, they populate a small central region. This causes most subclusters to pass through each other nearly simultaneously (or in a few lots). During this phase and in subsequent passages, the subclusters’ orbital kinetic energy (K.E.) is dissipated into the orbital energy of the individual stars via two-body energy exchange among the latter. This causes the subclusters’ orbits to sink towards the potential minimum (typically in a few orbits) where most of the stellar orbits confine forming an initially irregular and substructured stellar distribution. The redistribution of the stellar orbits of this stellar system drives it towards its lowest energy configuration (the “violent relaxation” process) causing its morphology to become increasingly spherically symmetric and the substructures to vanish. The infall and the initial merger processes occur in the dynamical time of the subclusters falling in the global potential well. As the newly merged system smoothes out and approaches dynamical equilibrium, the redistribution proceeds with the dynamical timescale of its stellar orbits.

The subclusters’ infall time, t_{in} , nevertheless serves as a lower limit of their merger time. An estimate of t_{in} is the “crossing time” over R_0 with the typical orbital velocity, σ_{in} , of a subcluster. An estimate of σ_{in} is the velocity dispersion needed to keep the system of subclusters, treated as point masses, in virial equilibrium. The virial theorem¹ then gives,

assuming no background gas,

$$\sigma_{in} \approx \sqrt{\frac{GM_*}{R_0}}.$$

Hence,

$$t_{in} = \frac{R_0}{\sigma_{in}} \approx \frac{R_0^{\frac{3}{2}}}{\sqrt{GM_*}}. \quad (1)$$

With a background residual gas of total mass M_g within R_0 , Eqn. 1 can be simply generalized to

$$t_{in} \approx \frac{R_0^{\frac{3}{2}}}{\sqrt{GM_{tot}}} = 0.152 \frac{\left(\frac{R_0}{\text{pc}}\right)^{\frac{3}{2}}}{\left(\frac{M_{tot}}{10^4 M_\odot}\right)^{\frac{1}{2}}} \text{ Myr}, \quad (2)$$

where $M_{tot} = M_* + M_g$. Note that Eqn. 2 is valid if the initial relative velocities of the subclusters are small compared to σ_{in} as in the present case (see Sec. 2.1).

Notably, t_{in} estimates only the *time of the first arrival* of the subclusters at their pericenters. As discussed above, the time taken to merge the subclusters into a single cluster in virial equilibrium can be substantially longer than t_{in} . This additional time, in which the subclusters’ orbit collapse towards the global potential minimum and the resulting stellar system eventually arrives at a featureless (near) spherically symmetric configuration (see above), can be referred to as the systemic violent relaxation time, t_{vrx} . t_{vrx} also scales with R_0 since increasing R_0 increases the amount of the subclusters’ orbital energy, which needs to be dissipated (see above). This orbit-shrinkage phase of the subclusters and hence t_{vrx} is too complicated to estimate analytically since the energy exchange process significantly deforms the subclusters from spherical symmetry and hence complicates the exchange itself. A direct N-body computation, as we do here with NBODY6 (see above), is the most reliable and accurate method to treat the merger process after time $t \gtrsim t_{in}$. Fig. 3 shows the dependence of t_{in} on typical masses and sizes involved in massive stellar associations. The thick curves correspond to the presently adopted values, *viz.*, $M_{tot} = (3 \times) M_* = (3 \times) 10^4 M_\odot$ (with) without the background gas.

The final radius, R_* , of the post-merger virialized cluster can also be estimated as follows which would be useful. To the lowest order, the length scale of the individual subclusters can be simply related to that of the final merged cluster in dynamical equilibrium. For purposes of estimates, we consider all subclusters having mass $m_{cl}(0) = M_{cl}$ and virial radius R_{cl} . For a Plummer cluster, R_{cl} is close to its half-mass radius $r_h(0)$. The total (kinetic + potential) energy of an individual Plummer (sub-) cluster is,

$$E_{cl} = \frac{V}{2} \approx -\frac{M_{cl}^2}{2R_{cl}},$$

where V is the total potential energy (P.E.) of the cluster. The G -constant is omitted in the following derivation since it would cancel out (see below).

Hence, for an ensemble of n clusters relatively at rest and uniformly distributed over a sphere of radius R_0 , as is

¹ A system is said to be in dynamical equilibrium if its statistical or “macroscopic” properties remain invariant with time or changes quasi-statically. According to the virial theorem, for a

self-gravitating system in dynamical equilibrium having a total K.E. T and P.E. V , $2T = -V$.

true for the current initial conditions (see Sec. 2.1), the total energy of the system is

$$E_{ini} \approx -\frac{nM_{cl}^2}{2R_{cl}} - \frac{n^2M_{cl}^2}{R_0}. \quad (3)$$

Here, $M_* = nM_{cl}$ is the total stellar mass. The second term in the right hand side (R.H.S.) of Eqn. 3 is the P.E. corresponding to M_* distributed uniformly over a sphere of radius R_0 and estimates the mutual P.E. of the subclusters. The corresponding K.E. term is zero since the subclusters have zero relative velocities. If the virial radius of the final merged stellar system of mass M_* is R_* , then the corresponding total energy is

$$E_{fnt} \approx -\frac{n^2M_{cl}^2}{2R_*}. \quad (4)$$

Here we take the fraction of stars that becomes unbound during the merger process (and by the dynamical evolution of the individual subclusters) to be negligible as confirmed in our computations (see below). The conservation of energy implies

$$E_{ini} = E_{fnt}.$$

Then Eqns. 3 & 4 give, after dividing by $n^2M_{cl}^2$,

$$\frac{1}{2R_*} \approx \frac{1}{2nR_{cl}} + \frac{1}{R_0}, \quad (5)$$

which is independent of the systemic stellar mass M_* . With a time-independent external potential, Eqn. 5 also holds true. Note that in the above calculation we ignore the corrections in the total energy due to the mutual tidal forces and hence Eqn. 5 is correct up to only the leading orders.

Table 3 summarizes the evolution (in Myr) of the subcluster systems of type A and B (see Sec. 2.1) initiating with increasing R_0 and in presence (for $\epsilon \approx 0.3$; see Sec. 2.2) and absence of a gas potential. These are computed using NBODY6 (see above). For the ease of description, the evolving morphologies of the stellar systems are divided into four categories as given in Table 2. As seen in Table 3, all computed configurations initiate as SUB and evolve via the intermediate CHas phase to the final CH cluster in dynamical equilibrium. In the CHas state, the stellar system has an overall core-halo structure but it is out of equilibrium and approaches dynamical equilibrium on the timescale of its typical stellar orbits².

As expected, configurations with smaller R_0 tend to merge quicker, as can be read from Table 3. For $R_0 \lesssim 1$ pc, the system attains a CH structure in $t \lesssim 1$ Myr without a gas potential. This is demonstrated in Fig. 4 (panels 1-3) where the initial system falls in from $R_0 = 1.1$ pc. On the other hand, initially wider configurations in Table 3 are all still SUB at $t = 1$ Myr even with the background gas potential and most of them do not attain the CH phase even in 2 Myr. An example is shown in Fig. 4 (panels 4-6).

Fig. 5 shows the snapshots at $t \approx 1$ Myr for a set of A-type configurations (systems A*b; see Tables 3 & 5) falling from increasing R_0 (without background gas potentials). With increasing R_0 , the morphology at 1 Myr changes from being CH, CHas to SUB. For $R_0 \gtrsim 2$ pc, the stellar system at

1 Myr substantially deviates from spherical symmetry (and dynamical equilibrium). Fig. 6 demonstrates the same for A- and B-type configurations with the more compact initial subclusters (systems A*a and B*a; see Tables 3 & 5). Note that the infall time, t_{in} , for $R_0 \approx 2$ pc ($M_{tot} \approx 10^4 M_\odot$) is much less than 1 Myr, as can be read from Fig. 3. This demonstrates the significance of the systemic violent relaxation time, t_{vrx} , beyond t_{in} (see above) which delays the appearance of the virialized merged cluster for $t > 1$ Myr, in this case.

Interestingly, the presence of a gas potential (Sec. 2.2) does not necessarily facilitate the approach to the CH morphology, as can be seen from Table 3. Although the gas potential causes the subclusters to make the first passage through each other (near their orbital pericenters) quicker (*i.e.*, makes t_{in} smaller; see Eqn. 2), they also approach faster than what they would have under just their mutual gravity. Hence a larger number of orbits are needed to dissipate the subclusters' orbital K.E. to that of the stars (see above). In other words, the addition of a gas potential tends to lengthen t_{vrx} without increasing R_0 . For $R_0 \gtrsim 2$ pc, it takes longer to arrive at the CH state with the gas background than without as seen in the present N-body calculations. Hence, the ‘‘conveyor belt’’ mechanism (Longmore et al. 2014), in fact, tends to delay the assembly of the final star cluster. This, of course, depends on the gas mass (potential) in the system relative to the stellar mass. A detailed quantification of the role of the background gas in the subcluster merger timescale is reserved for a future paper.

Furthermore, systems with similarly massive but less compact subclusters generally take longer to merge as can be inferred from Table 3. The times at which the subclusters with $r_h(0) = 0.1$ pc combine to form an equilibrated CH structure, those with $r_h(0) = 0.3$ pc are still in CHas state. More compact subclusters have higher stellar densities which cause their orbital energy dissipation to be more efficient as they pass through each other at the beginning of the merger process (see above).

Figs. 7 & 8 show examples of infall from $R_0 = 5$ pc and 10 pc respectively comparing between the cases with and without the background gas. The systems are still highly SUB at 2 & 3 Myr respectively (the $R_0 = 5$ pc systems become CH by 3 Myr). The faster initial collapse in presence of the gas potential can also be vividly seen in these figures. In panel 3 of Fig. 7 ($R_0 = 5$ pc), *i.e.*, with the gas potential, the stellar system is close to its first mutual (pericenter) passage at $t \approx t_{in} \approx 1$ Myr and spreads out further after a Myr (panel 4). The first mutual passage occurs at $t \approx t_{in} \approx 2$ Myr without the gas potential for the same stellar system (panel 2). These times are close to what one expects from the analytic estimate of t_{in} for $R_0 \approx 5$ pc in Fig. 3 (*c.f.* the highlighted curves in this figure). Similarly, for $R_0 = 10$ pc, the stellar system is close to its first pericenter at $t \approx 3$ Myr (panel 4 of Fig. 8) with the gas potential but far from reaching there without it (panel 2), as can be expected from Fig. 3. Notably, the tidal field due to the background potential elongates the subclusters as can be seen in the panels 3 & 4 of Figs. 7 & 8.

In all the calculations reported here (both without and with gas potential), a negligible fraction of stars escape the system during the infall and the merger process. In other words, the total bound stellar mass M_* remains nearly un-

² This timescale is of the order of the crossing time of the final virialized cluster.

tered as the system evolves from its SUB to its CH morphology. In the panels of Figs. 2 - 8 only those stars are plotted which are gravitationally bound w.r.t. the entire system.

3.2 Structure of the assembled star cluster: comparison with NGC 3603 young cluster

To obtain an HD97950-like star cluster by hierarchical merging of subclusters, the necessary but not sufficient condition is to arrive at a CH configuration in $t \lesssim 1$ Myr. The calculations described in Sec. 3.1 imply that to have a CH morphology at 1 Myr, one should have $R_0 \lesssim 2$ pc with or without a gas potential (see Table 3 and Fig. 5). As discussed there, the presence of the gas potential would delay the appearance of the CH configuration. How does this final cluster compare with the observed HD97950 cluster?

Table 4 lists the best-fit parameters of the King surface mass-density (Σ_M) profile (King 1962; Heggie & Hut 2003) fitted to the observed Harayama et al. (2008) profile of HD97950. The set of values of the King concentration parameter k and the core-radius r_c , as in the first line of Table 4, is also quoted by Harayama et al. (2008)³. However, for the two innermost annuli of this profile, Σ_M fluctuates considerably (see fig. 14 of Harayama et al. 2008) indicating possible systematic and/or crowding effects. Hence we also quote the best-fitted King parameters in Table 4 (with similar χ^2) excluding either of the two innermost points, giving the limits of k . Note that the King tidal cutoff radius, r_t , is consistent with being very large for all the three fits and is nearly uncorrelated with k and r_c , implying that HD97950 is untruncated. In other words the cluster under-fills its Roche lobe (Jacobi radius) in the Galactic potential.

Table 5 shows the King best-fit parameters at $t \approx 1$ Myr for those gas-free systems which arrive at a CH morphology in $t \lesssim 1$ Myr, *i.e.*, for systems with $R_0 \lesssim 2$ pc. Although (near) spherical star clusters are formed by 1 Myr in these cases, they have much higher central concentrations (k) and/or larger cores (r_c) than what is observed for HD97950 (*c.f.* Table 4). This is demonstrated in Fig. 9. At $t \approx 1$ Myr, the overall density profiles of these merged CH clusters follow neither a Plummer nor a King profile strictly. Due to more freedom in parameters, the King surface density profile still fits reasonably with these configurations except over their outermost parts (see Table 5). Such fitted King profiles are usually truncated (*i.e.*, have finite r_t , unlike what is observed; see above) and fall below the computed profiles in their outer zones, typically beyond the vivid kink in their profiles (see Fig. 9) at around 40 - 60 arcsec (1.2 pc - 1.8 pc). This indicates that these outermost “halo” regions of these newly assembled systems are still in the process of integrating with their main clusters. Furthermore, in the outer radii, the computed density profiles typically fall below the observed profile as seen in Fig. 9, implying that the former are more compact. Note that in Fig. 9, all the computed and the observed profiles use the same radial bins and stellar mass range for direct comparison.

Note that the computed clusters in Table 5 are for $M_* \approx 10000M_\odot$ which is the lower mass limit of HD97950. As shown in Sec. 3.1 (see Eqn. 5), the length scale of the

final merged cluster, R_* , is nearly independent of the total stellar mass M_* . Hence, a stellar system with larger M_* would combine to a cluster of the same size, *i.e.*, it would be even more overdense compared to the observed HD97950⁴. The appearance of the centrally overdense assembly is irrespective of the initial mode of subclustering as it occurs for both type A and B systems with a range of masses and sizes of the subclusters (see Table 5).

As such, according to Eqn. 5, more extended (larger R_*) and hence less centrally dense assembly can be obtained starting with more extended subclusters (larger R_{cl}), for a given R_0 . However, our choice of the highly compact initial subclusters is dictated by the observed thinness of the dense molecular gas filaments (see Sec. 2.1). Also, under typical conditions, one would have $R_0 \gg R_{cl}$, making the first term in the R.H.S. of Eqn. 5 to be dominant (unless n is very large). Hence, if one relaxes the $t < 1$ Myr condition, *i.e.*, considers larger R_0 , one would still obtain similarly dense assemblies. Finally, according to Eqn. 5, R_* is independent of the background gas potential if the potential remains static during the infall and the subsequent merger process.

The newly assembled cluster can be more extended by including primordial binaries which “heats” the cluster via super-elastic binary-single star and binary-binary encounters (Heggie & Hut 2003). The merged cluster can also be heated and expanded by mass loss due to the stellar winds. As shown in the last section of Table 5, the stellar wind has a negligible effect on the merged CH system and the primordial binaries expand the cluster but insufficiently; *c.f.* values in Table 5 for similar configurations but without stellar evolution and primordial binaries. This is demonstrated in Fig. 10. As mentioned earlier, NBODY6 does not include PMS evolution, so we use its default MS wind which is strongest for the massive stars (the most massive star in the system is of $\approx 80M_\odot$). As for the primordial binaries, we use the “birth period distribution” (Kroupa 1995; Marks et al. 2014) as in Banerjee & Kroupa (2014), for each initial subcluster. Such initial binary population contains $\approx 40\%$ hard binaries.

3.2.1 Calculations including gas expulsion

One way to dramatically expand a star cluster, however, is to subject it to a substantial gas expulsion on a timescale of the order of its dynamical time, as discussed in Sec. 1. We repeat a subset of the calculations in Table 5 by initiating them in presence of Plummer gas potentials as described in Sec. 2.2. The gas potential is then diluted exponentially with time, mimicking gas expulsion (see Sec. 2.2). The timescales defining the potential depletion are taken to be the same representative values as in Banerjee & Kroupa (2014). Specifically, the gas cloud starts to expel after a delay time $\tau_d \approx 0.6$ Myr, after it is ionized by the UV radiation from the massive stars, with the HII sound speed of $v_g \approx 10$ km s⁻¹. This gives a decay timescale of $\tau_g = R_0/v_g$. As discussed in Banerjee & Kroupa (2014), these timescales are only representatives but consistent with recent theoretical studies on ultra-compact HII regions. As discussed in

⁴ A system with larger M_* would also take longer to merge since a larger amount of orbital energy needs to be dissipated (see Sec. 3.1).

³ $1'' \approx 0.03$ pc at the distance of NGC 3603.

Sec. 2.2, the total gas mass within R_0 is chosen to be $2M_*$ so that the local SFE $\approx 33\%$. This SFE is consistent with both theoretical studies and observations.

The columns 1 & 2 of Table 6 give the 4 computed configurations which are subjected to residual gas dispersal in the above way. The final calculation also includes primordial binaries (see above). All these configurations arrive at a CH state by $t \lesssim 0.4$ Myr, *i.e.*, well before the commencement of gas dispersal at $t \approx 0.6$ Myr⁵. Fig. 11 shows the corresponding stellar mass-density profiles at $t \approx 1$ Myr. As demonstrated there, they agree reasonably with the observed profile of HD97950 (Harayama et al. 2008), particularly in the inner regions. The King best-fit parameters for these profiles are given in Table 6 which agree fairly with those of the observed ones. In particular, these profiles are consistent with being untruncated monolithic profiles (*i.e.*, they have large r_t), as observed, and unlike those obtained in the absence of gas dispersal (*i.e.*, without any gas potential; see above). See the notes in Table 6 for additional clarifications. Note that in Fig. 11, the “natural” matchings with the observed profile are obtained *by simply overlaying it with the computed profiles at 1 Myr without any scaling or fitting*, as in Banerjee & Kroupa (2014). As in Figs. 9 and 10, the same radial bins and stellar mass range are used to construct the observed and the computed profiles in Fig. 11.

Fig. 12 shows the evolution of 1-dimensional velocity dispersion, σ_{1d} , for the computations corresponding to Fig. 11. In all cases, the σ_{1d} components within the central $R < 0.5$ pc ($R \lesssim 15''$) of the star cluster, for $1.7 - 9.0M_\odot$ stars, lie between $3.0 - 4.0$ km s⁻¹ at $t \approx 1$ Myr. These values are somewhat smaller than what is observed for the same region and stellar mass range in HD97950 (Rochau et al. 2010), *viz.*, $\sigma_{1d} = 4.5 \pm 0.8$ km s⁻¹ (mean over two orthogonal components). Pang et al. (2013) report a substantial spread among the σ_{1d} components, *viz.*, $4.5 - 7.0$ km s⁻¹ which is larger than what is obtained in the above calculations. This is unlike the case of monolithic cluster-formation model in Banerjee & Kroupa (2014) where the Σ_M profile as well as the σ_{1d} s from the same computed model agree with those observed for HD97950.

In fact, the central σ_{1d} s in the present calculations are smaller than those in Banerjee & Kroupa (2014) throughout the evolution. This can be attributed to the smaller central concentrations of the assembled pre-gas-expulsion CH clusters here, than that of the Banerjee & Kroupa (2014) monolithic embedded cluster (which corresponds to $k \approx 40$, $r_c \approx 2''$). Note that the total stellar mass of the pre-gas-expulsion cluster $M_* \approx 10000M_\odot$ for both cases. To obtain a similarly concentrated assembled cluster, the initial subclusters should have been much more concentrated (Eqn. 5). The smallest sized subclusters in the calculations in Table 6 have scale length $r_h(0) \approx 0.1$ pc; this is the peak of the narrow distribution of the widths of molecular gas filaments (André et al. 2011). Hence taking all subclusters substantially more compact would not correspond to a realistic situation.

For the sake of argument, even if one considers such

an initial condition, the subsequent gas expulsion would yield a cluster which is centrally overdense w.r.t. HD97950 even for its above lower mass limit. This is because the currently computed models in Table 6 already yield the right central density and the latter quantity scales with its pre-gas-expulsion value. As argued in Banerjee & Kroupa (2014), moderate variations of the SFE or the gas dispersal timescales would not mend this since at $t \approx 1$ Myr all stars are still in the central region of the expanding system and are always intercepted in the density profile. A similar line of argument applies if one considers a larger M_* . Notably, the expansion of the merged cluster after the gas expulsion and hence the corresponding decline of σ_{1d} occur to a smaller extent in the present calculations than those in Banerjee & Kroupa (2014) (*c.f.* Fig. 12 here and Fig. 3 of Banerjee & Kroupa 2014). This is because the gas (potential) of the same mass $2M_*$ is much more spread out over the length scale $R_0 > R_*$ in the present case than in Banerjee & Kroupa (2014) where the gas follows the highly compact pre-gas-release cluster profile (see above). Hence, the latter is subjected to significantly more central mass loss than the present pre-gas-release clusters. The above discussion implies that the combination of the physically motivated initial conditions adopted here optimally reproduces the observed mass density profile of HD97950.

4 CONCLUSIONS, DISCUSSIONS AND OUTLOOK

The primary objective of the calculations described in the previous sections is to find initial conditions under which it is feasible to assemble a VYMC like the HD97950 from an initial distribution of subclusters, given the mass and age constraints for this cluster. The key inferences can be summarized as follows:

- A system of subclusters of total stellar mass $M_* \approx 10^4 M_\odot$ assemble into a (near) spherical core-halo star cluster by the age of HD97950 (*i.e.*, in $t < 1$ Myr) provided these subclusters are largely born over a region of scale length more compact than $R_0 \lesssim 2$ pc. This can happen, *e.g.*, in an intense starburst event at a dense “spot” in a molecular cloud.
- The initial sizes of the subclusters are constrained by the highly compact sections of molecular gas filaments or filament junctions which, in turn, determines the compactness of the final assembled cluster. The size of the final cluster is also independent of the presence of residual molecular gas. Therefore, the mass density over the central region (within a virial radius) of the merged cluster is determined by the total stellar mass that is involved in its assembly.
- A “dry” merger of subclusters, *i.e.*, infall in absence of residual molecular gas (all gas consumed into stars) always leads to a star cluster that is centrally overdense w.r.t. HD97950, even for the latter’s lower mass limit $M_* \approx 10^4 M_\odot$. This is irrespective of the initial mode of subclustering. The expansion of the final cluster due to stellar winds and primordial binaries is insufficient, as indicated by the present calculations.
- A substantial residual gas expulsion ($\approx 70\%$) occurring after the formation of the merged cluster expands the latter to obtain a cluster profile that is consistent with

⁵ Test calculations are also done when the gas expulsion is initiated as early as during the initial infall process, well before the CH phase. This typically leads to the dispersal of most of the subclusters instead of merging into a single cluster.

the observed HD97950. With the lower stellar mass limit $M_* \approx 10^4 M_\odot$ and an SFE of $\epsilon \approx 30\%$, the observed surface mass density profile of HD97950 can be fairly and optimally reproduced although the central velocity dispersion falls short by $\approx 1 \text{ km s}^{-1}$.

- In principle, with more extended initial subclusters it is possible to obtain a merged profile that agrees with that observed for HD97950, without any gas dispersal (*i.e.*, via dry mergers). However, the resulting central velocity dispersion would then be even lower than the observed value. Much extended subclusters are as well inconsistent with the highly compact widths of molecular gas filaments.

- Hence, *the NGC 3603 young cluster (HD97950) has formed essentially monolithically followed by a substantial gas dispersal. The initial monolithic stellar distribution has either formed in situ or has been assembled promptly (in $\lesssim 1 \text{ Myr}$) from closely packed (within $\lesssim 2 \text{ pc}$) less massive stellar clusters (subclusters). Both scenarios are consistent with the formation of HD97950's entire stellar population in a single starburst of very small duration.* The in-situ scenario (Banerjee & Kroupa 2014) seems to better reproduce the observed properties of HD97950.

A key concern in the above conclusion is that such closely packed gas-embedded subclusters are *usually* not seen in practice. This further supports the in-situ formation of young massive clusters. However, this does not rule out the prompt assembly channel either. The initial closely packed subcluster distribution has a very short lifetime and it merges to a single (embedded) core-halo structure in a fraction of a Myr. Hence such systems should be rare to observe. Notably, recent multi-wavelength observations of the Pismis 24 cluster of NGC 6357 (Massi et al. 2014) indicate that this young cluster (age 1-3 Myr) contains distinct substructures which must have formed out of dense gas clumps packed within $\approx 1 \text{ pc}$ radius. Using the MYStIX survey catalog, Jaehnig et al. (2014) also find that the stellar distribution in young clusters (1-3 Myr) tend to smoothen out with age and local stellar density. This indicates an appearance of these systems as closely packed stellar overdensities which disappear on a dynamical timescale as seen in the calculations described in the above sections.

Also, the requirement of substantial ($\approx 70\%$ by mass) gas expulsion is supported by the lack of gas in young and intermediate-aged clusters. In particular, a recent survey of the LMC's massive star clusters over wide ranges of mass ($> 10^4 M_\odot$) and age (30-300 Myr) has failed to identify reserved gas in any of these clusters (Bastian & Strader 2014). These clusters would have accreted enough surrounding gas by now for the latter to be detected inside them. This implies that star clusters can, in fact, disperse their gaseous component efficiently at any age $< 300 \text{ Myr}$ and irrespective of their escape velocities (Bastian & Strader 2014).

The primary simplification in the above study is the analytic treatment of the residual gas that forms a spherically symmetric smooth Plummer profile (see Sec. 2.2). The gas consumption by the star formation process in the vicinity of the individual subclusters would imprint a “swiss-cake” structure in the spatial distribution of the density of the residual gas. Furthermore, the residual gas cloud could still develop filamentary overdensity structures across it. Hence an infalling subcluster is susceptible to tidal shocks that

accelerate its disruption. This detail is not critical for the present conclusions since the tidal field due to the background smoothed gas potential already disrupts the subclusters significantly during their infall, as seen in the above calculations.

It is rather surprising that despite the wide variety of initial conditions (*c.f.* Table 6) and the simplistic treatment of gas expulsion, the density profile of HD97950 is reproduced naturally in each case. This is as well true for the in-situ model of Banerjee & Kroupa (2014). As explained there, this implies that the analytic formulation aptly describes the bulk dispersal of the residual gas. The complex details of matter-radiation interaction and localized processes (*e.g.*, turbulence, instabilities and outflows) seemingly do not affect the release of the bulk of the gas from the system. That the dynamic expulsion of gas, as modelled using the SPH method, reproduces the here-used analytical time variation has indeed been demonstrated by Geyer & Burkert (2001).

The use of initially spherical subclusters (with or without the gas potential) is also an idealization since a newly hatched group of stars would preferentially follow its local gas overdensity pattern. However, the stellar assembly would become spherical (ellipsoidal in presence of gas potential) in a few of its dynamical times. For a stellar assembly as compact as the gas filaments, its internal dynamical time is typically much shorter than that of its infall. This effectively reduces a more realistic system to the idealized initial condition adopted here. For a sufficiently small initial span (*e.g.*, for the smallest R_0 used here; *c.f.* panels 2 & 3 of Fig. 2), the two timescales are comparable and the whole system can be considered to approach spherical symmetry (and dynamical equilibrium) in a single dynamical timescale. In that case the geometry of the individual subclusters does not play a role.

It is also possible that the individual subclusters collect a substantial fraction of the residual molecular gas during their migration towards the global potential minimum. Additionally, gas can be streamed towards the global potential minimum. Such cooling flows become efficient if the gas is sufficiently cold. In that event the assembled system will have the gas following the stellar distribution closely unlike the present case (see Sec. 3.2.1). Hence the system reduces to a monolithic “initial” condition as in Banerjee & Kroupa (2013, 2014) for which there exists a solution that matches well with HD97950 (Banerjee & Kroupa 2014).

In the present study, $t \approx 1 \text{ Myr}$ is considered as a “deadline” for cluster formation (see above) since the focus here is on the formation of HD97950. The zero age is the beginning of the dynamical evolution (or of the N-body calculations), which corresponds to the epoch of the formation of the subclusters in a single starburst. The concurrent appearance of subclusters, *i.e.*, a single starburst of very small or zero age spread giving rise to a subclustered configuration, is plausible only in a sufficiently compact region. The more extended the star-bursting region is (*i.e.*, the larger is R_0), a correlation is necessary over larger distances which makes such an event increasingly less probable. Hence, the prompt assembly or the compact in-situ formation are consistent with both the inferred young age and the very small age spread of HD97950. Note that $t \approx 1 \text{ Myr}$ does not represent any fundamental deadline; it is used here to narrow down the initial conditions.

The present calculations imply that although VYMCs can form as highly substructured (or fractal) stellar distributions, they still undergo a much more compact (and hence dense) phase than their present-day state. Hence, an initial primordial binary population would be substantially more dynamically processed (Marks & Kroupa 2012) than what has been suggested recently by Parker (2014), since the computed systems in the latter study do not necessarily go through a dense enough phase.

A straightforward leap in the present line of study is to conduct a more thorough survey of the merger time as a function of M_* , R_0 and ϵ , irrespective of any deadline. It is as well necessary to quantitatively relate the structure of the final cluster with these parameters and also with the sizes of the initial subclusters. Such a survey would be applicable to VYMCs in general. The detail of such modelling can be improved in future by introducing PMS evolution recipes and primordial binaries.

Another important improvement would be to do a detailed structural analysis of the final merged system. In particular, the construction of adaptive surface density maps, as in Kuhn et al. (2014), can be applied to the computed merged systems. This would determine their sphericity accurately or reveal if they still contain substructures at a given age. By comparing with the density patterns of observed VYMCs as in Kuhn et al. (2014), it would be possible to constrain the initial conditions of these VYMCs. In this context, it would be worthwhile to obtain such density contours for the observed HD97950 cluster as well in order to determine whether it harbours substructures. This would further constrain the conditions at its birth.

It is currently technologically formidable to form the subclusters from ab-initio hydrodynamic calculations for the present mass scale ($> 10^4 M_\odot$). However, in the foreseeable future, it would be possible to treat the residual gas hydrodynamically that can be energized by an appropriately modelled stellar feedback. This is possible to achieve by, *e.g.*, using the “AMUSE” framework (Portegies Zwart et al. 2008). In this way the gas expulsion process can be treated in a more realistic but technologically accessible manner (Simon Portegies Zwart; private communications). The timescale of the dispersal would, of course, depend on the modelling of the stellar feedback.

The above discussions imply that although simplifications and idealizations are adopted in the present study, they do not alter the key conclusions and their interrelations as enlisted above, namely, that the evidence points towards VYMCs such as HD97950, R136, the ONC and the Pleiades having formed essentially monolithically with substantial gas expulsion. Future unprecedented resolution of molecular cloud filaments and filament junctions with *ALMA* and proper motion measurements of the stars in the outer regions of young star clusters with *Gaia* (see Banerjee & Kroupa 2014) will provide more direct tests of such birth environments of VYMCs.

ACKNOWLEDGEMENTS

The authors are thankful to Pau Amaro-Seoane of the Albert Einstein Institute, Potsdam, Nate Bastian of the Liverpool John Moores University, Roberto Capuzzo-Dolcetta

of the La Sapienza University, Rome, Mike Fellhauer of the University of Concepcion and Adam Grinsberg of the European Southern Observatory, Garching for useful comments and criticisms. The authors are thankful to the anonymous referee for the suggestions which have improved the presentation of the paper.

REFERENCES

- Aarseth, S.J. 2003, “Gravitational N-Body Simulations”. Cambridge University Press.
- Adams, F.C. 2000, *ApJ*, 542, 964.
- Alves, J. and Bouy, H. 2012, *A&A*, 547, A97.
- Amaro-Seoane, P., Konstantinidis, S., Freitag, M.D., et al. 2014, *ApJ*, 782, 97.
- André, P., Meñshchikov, A., Koenyves, V., et al. 2011, in Alfaro Navarro, E.J., Gallego Calvente, A.T., Zapatero Osorio, M.R. (Eds.) *Stellar Clusters & Associations: A RIA Workshop on Gaia*. Granada, Spain: IAA-CSIC, 321.
- Banerjee, R. 2014, *A&A* submitted, arXiv:1409.7584 (preprint).
- Banerjee, S. and Kroupa, P. 2013, *ApJ*, 764, 29.
- Banerjee, S. and Kroupa, P. 2014, *ApJ*, 787, 158.
- Bastian, N. and Strader, J. 2014, *MNRAS*, arXiv:1407.2726 (preprint).
- Bate M.R. and Bonnell, I.A. 2004, in Lamers, H.J.G.L.M., Smith, L.J., Nota A. (Eds.) *The Formation and Evolution of Massive Young Star Clusters*, (ASP Conf. Proc. 322). San Francisco: Astronomical Society of the Pacific, 289.
- Bate M.R., 2009, *MNRAS*, 392, 590.
- Bate, M.R. 2012, *MNRAS*, 419, 3115.
- Bate, M.R., Tricco, T.S., Price, D.J. 2014, *MNRAS*, 437, 77.
- Baumgardt, H. and Kroupa, P., 2007, *MNRAS*, 380, 1589.
- DeRose, K.L., Bourke, T.L., Gutermuth, R.A., et al. 2009, *AJ*, 138, 33.
- Feigelson, E.D., Townsley, L.K., Broos, P.S., et al. 2013, *ApJS*, 209, 26.
- Fujii, M.S., Saitoh, T.R. and Portegies Zwart, S.F. 2012, *ApJ*, 753, 85.
- Geyer, M.P. and Burkert, A. 2001, *MNRAS*, 323, 988.
- Girichidis, P., Federrath, C., Banerjee, R. and Klessen, R.S. 2011, *MNRAS*, 413, 2741.
- Girichidis, P., Federrath, C., Allison, R., et al. 2012, *MNRAS*, 420, 3264.
- Harayama, Y., Eisenhauer, F. and Martins, F. 2008, *ApJ*, 675, 1319.
- Heggie, D.C. and Hut, P. 2003, “The Gravitational Millon-Body Problem: A Multidisciplinary Approach to Star Cluster Dynamics”. Cambridge University Press, Cambridge, UK.
- Hurley, J.R., Pols, O.R. and Tout, C.A. 2000, *MNRAS*, 315, 543.
- Jaehnig, K.O., Da Rio, N. and Tan, J.C. 2014, arXiv:1410.4197 (preprint).
- King, I. 1962, *AJ*, 67, 471.
- Klessen, R.S., Burkert, A. and Bate, M.R. 1998, *ApJ*, 501, L205.
- Kroupa, P. 1995, *MNRAS*, 277, 1507.
- Kroupa, P. 2001, *MNRAS*, 322, 231.

- Kroupa, P., Aarseth, S. and Hurley, J. 2001, *MNRAS*, 321, 699.
- Kroupa, P. and Bouvier, J. 2003, *MNRAS*, 346, 343.
- Kroupa, P., et al. 2013, in Oswalt, T.D. and Gilmore, G. (Eds.) *Galactic Structure and Stellar Populations* (Planets, Stars and Stellar Systems, Volume 5). Springer Science+Business Media Dordrecht (2013).
- Küpper, A.H.W., Maschberger, T., Baumgardt, H. and Kroupa, P. 2011, *MNRAS*, 417, 2300.
- Kuhn, M.A., Feigelson, E.D., Getman K.V., et al. 2014, *ApJ*, arXiv:1403.4252 (preprint).
- Lada, C.J. and Lada, E.A. 2003, *ARA&A*, 41, 57.
- Longmore, S.N., Kruijssen, J.M.D., Bastian, N., et al. 2014, in Beuther, H., Klessen, R., Dullemond, C. and Henning, Th. (Eds.) *Protostars and Planets VI*, University of Arizona Press, preprint (arXiv:1401.4175).
- Machida, M.N. and Matsumoto, T. 2012, *MNRAS*, 421, 588.
- Malinen, J., Juvela, M., Rawlings, M.G., et al. 2012, *A&A*, 544, A50.
- Marks, M. and Kroupa, P. 2012, 543, A8.
- Marks, M., Leigh, N., Giersz, M., et al. 2014, *MNRAS*, 441, 3503.
- Massi, F., Giannetti, A., di Carlo, E. 2014, *A&A*, arXiv:1410.4340 (preprint).
- Palla, F. and Stahler, S.W. 2002, *ApJ*, 581, 1194.
- Pang, X., Grebel, E.K., Allison, R., et al. 2013, *ApJ*, 764, 73.
- Parker, R.J. 2014, *MNRAS*, 445, 4037.
- Pfalzner, S. and Kaczmarek, T. 2013, *A&A*, 555, A135.
- Plummer, H.C. 1911, *MNRAS*, 71, 460.
- Portegies Zwart, S.F., McMillan, S.L.W., Nualláin, B. Ó., et al. 2008, *Lecture Notes in Computer Science*, 5102, 207.
- Portegies Zwart, S.F., McMillan, S.L.W. and Gieles, M. 2010, *ARA&A*, 48, 431.
- Price, D.J. and Bate, M.R. 2010, in *Plasmas in the laboratory and the Universe: Interactions, Patterns, and Turbulence*, (AIP Conf. Proc. 1242), 205.
- Rochau, B., Brandner, W., Stolte, A., Gennaro, M., et al. 2010, *ApJ*, 716, L90.
- Schneider, N., Csengeri, T., Bontemps, S., et al. 2010, *A&A*, 520, A49.
- Schneider, N., Csengeri, T., Hennemann, M., et al. 2012, *A&A*, 540, L11.
- Smith, R., Goodwin, S., Fellhauer, M. and Assmann, P. 2013, *MNRAS*, 428, 1303.
- Stolte, A., Brandner, W., Brandl, B., et al. 2004, *AJ*, 128, 765.
- Stolte, A., Brandner, W., Brandl, B., et al. 2006, *AJ*, 132, 253.
- Weidner, C. and Kroupa, P. 2004, *MNRAS*, 348, 187.
- Weidner, C. and Pflamm-Altenburg, J. 2013, *MNRAS*, 434, 84.
- Wright, N.J., Parker, R.J., Goodwin, S.P. and Drake, J.J. 2014, *MNRAS*, 438, 639.

Table 1. Parameters of the NGC 3603 Young Cluster (HD 97950) as determined from observations.

Quantity	Measurement	Value(s)	Reference(s)
Mass M_*	Photometry	$(1.0 - 1.6) \times 10^4 M_\odot$	Stolte et al. (2006); Harayama et al. (2008)
Mass M_*	Kinematics	$(1.7 - 1.9) \times 10^4 M_\odot$	Rochau et al. (2010); Pang et al. (2013)
Age	Photometry	1 Myr	Stolte et al. (2004); Pang et al. (2013)
Velocity dispersion σ_{1d} (mean 1-d)	Proper motion	$4.5 \pm 0.8 \text{ km s}^{-1}$	Rochau et al. (2010)
Velocity dispersion σ_{1d} (orthogonal 1-d)	Proper motion	$(4.8 - 6.5) \pm 0.5 \text{ km s}^{-1}$	Pang et al. (2013)
Central concentration parameter k	King/EFF profile fit ^a	4.2	Harayama et al. (2008)
Core radius r_c	King/EFF profile fit	$4.8'' (\approx 0.15 \text{ pc})$	Harayama et al. (2008)
Tidal radius r_t	King/EFF profile fit	large	Harayama et al. (2008)
Distance from the Sun	Photometry	$6.0 \pm 0.8(0.3) \text{ kpc}$	Harayama et al. (2008) (Stolte et al. 2004)

^a The theoretical King (also Elson-Fall-Freeman or EFF) profiles are best-fitted with the observed surface mass density profile of HD 97950 for the stellar mass range $0.5 - 2.5 M_\odot$. See also Table 4.

Table 2. A basic classification of the different morphologies in the spatial distribution of stars that can occur in the process of subcluster merging. These morphologies appear in the models computed here. Note that the distinctions among these morphologies are only qualitative for the present purpose and are made for the ease of descriptions.

Morphology	Abbreviation	Example
Substructured	SUB	Fig. 2
Core + asymmetric and/or substructured halo	CHas	Fig. 5, panels 3,4
Core-halo with near spherical symmetry	CH	Fig. 4, panel 3
Core + halo containing satellite clusters	CHsat	Fig. 7, panel 4

Table 3. An overview of the evolutionary sequences of the primary systems as computed here. A particular row indicates how the morphology (see Table 2) of the corresponding system evolves with evolutionary time (in Myr as indicated by the numerical values along the columns 3-5 and 6-8), for systems both without and with a background gas potential (see text). As expected, the systems, in general, evolve from substructured to a core-halo configuration with a timescale that increases with increasing initial extent R_0 . See text for details.

Config. name	Short name	Without gas potential			With gas potential ($\epsilon \approx 0.3$)		
m1000r0.1R1.1N10 ^a	A-Ia	0.2,SUB	0.6,CHas	1.0,CH	0.2,SUB	0.6,CHas	1.0,CH
m1000r0.3R1.1N10	A-Ib	0.2,SUB	0.6,CHas	1.0,CHas	0.2,SUB	0.6,CHas	1.0,CHas
m1000r0.1R2.5N10	A-IIa	0.6,SUB	1.0,SUB	2.0,CH	0.6,SUB	1.0,CHsat	2.0,CHas
m1000r0.3R2.5N10	A-IIb	0.6,SUB	1.0,SUB	2.0,CHas	0.6,SUB	1.0,CHsat	2.0,CHas
m10-150r0.01-0.1R1.1N150 ^b	B-Ic	0.2,SUB	0.6,CHas	1.0,CH	0.2,SUB	0.6,CHas	1.0,CHas
m10-150r0.1R1.1N150	B-Ia	0.2,SUB	0.6,CHas	1.0,CH	0.2,SUB	0.6,CHas	1.0,CHas
m10-150r0.1R2.5N150	B-IIa	0.6,SUB	1.0,SUB	2.0,CHas	0.6,SUB	1.0,CHas	2.0,CHas
m1000r0.5-1.0R5.0N10	A-IIIc	1.0,SUB	2.0,SUB	3.0,CHas	1.0,CHsat	2.0,CHsat	3.0,CHsat
m1000r0.5-1.0R10.0N10	A-IVd	1.0,SUB	2.0,SUB	3.0,SUB	1.0,SUB	2.0,SUB	3.0,CHsat

^a $mzryRzNn$ implies an initial system (at $t = 0$) comprising of $N = n$ Plummer clusters, each of mass $m = m_{cl}(0) = xM_\odot$ and half-mass radius $r = r_h(0) = y \text{ pc}$, distributed uniformly over a spherical volume of radius $R = R_0 = z \text{ pc}$.

^b Further, when a range of values $x1 - x2$ is used instead of a single value, it implies that the corresponding quantity is uniformly distributed over $[x1, x2]$ at $t = 0$.

Table 4. Best-fit parameters for the King surface mass-density profile with that observed for the NGC 3603 young cluster (Harayama et al. 2008).

Data included	k	$r_c(\prime\prime)$	$r_t(\prime\prime)$	χ^2
All	4.3 ± 0.6	4.8 ± 0.4	— ^b	1.5
All but 2nd annule ^a	3.8 ± 0.6	5.1 ± 0.4	— ^b	1.2
All but 1st annule ^a	5.8 ± 1.1	4.1 ± 0.4	— ^b	1.2

^a The measured projected mass-density profile of Harayama et al. (2008) shows substantial fluctuations among the innermost annuli. Equally good but fitted profiles of significantly different central concentrations (k) are obtained when each of the two innermost annuli are considered individually. At the distance of NGC 3603 $1'' \approx 0.03$ pc.

^b The King tidal radius (r_t) is large and does not affect the fit, implying a cluster profile with no tidal cut-off.

Table 5. Best-fit parameters for the King surface mass-density profile at $t \approx 1$ Myr for those computed configurations which evolve to form a star cluster with near-spherical core-halo structure (the CH-type morphology, see Table 2) within $t < 1$ Myr, in absence of a background gas potential. All of these profiles are much more concentrated and/or flattened than the observed profile of HD97950 (*c.f.* , Table 4) as is also evident from Fig. 9.

Config. name	Short name	k	$r_c(\prime\prime)$	$r_t(\prime\prime)$	χ^2	$R_{\text{lim}}(\prime\prime)^a$
m1000r0.1R0.5N10	A-0.5Ia	26.7	4.4	37.0	1.3	25
m1000r0.1R1.1N10	A-Ia	8.2	7.1	88.2	0.5	40
m1000r0.1R2.5N10	A-IIa	—	—	—	—	— ^b
m1000r0.3R0.5N10	A-0.5Ib	16.6	3.7	126.1	1.4	65
m1000r0.3R1.1N10	A-Ib	9.6	6.2	87.7	1.8	40
m1000r0.3R1.5N10	A-1.5Ib	10.3	7.2	57.7	1.1	40
m1000r0.3R2.0N10	A-2.0Ib	5.5	6.8	254.1	1.0	40
m1000r0.3R2.5N10	A-IIb	—	—	—	—	—
m10-150r0.01-0.1R1.1N150	B-Ic	9.3	7.2	85.3	1.7	65
m10-150r0.1R1.1N150	B-Ia	11.0	5.6	83.3	2.3	50
m10-150r0.1R2.5N150	B-IIa	—	—	—	—	—
m1000r0.3R0.5N10-se ^c	A-0.5Ib-se	17.7	3.5	137.0	2.2	65
m1000r0.3R1.1N10-pb ^c	A-Ib-pb	7.0	10.8	46.9	2.5	35
m10-150r0.1R1.1N150-se	B-Ia-se	10.3	6.2	77.0	2.0	55

^a R_{lim} is the distance from the cluster’s (density) center until which a reasonable King-profile fit to its surface density profile could be obtained.

^b The empty data lines indicate that a star cluster with a CH-type morphology cannot form within $t < 1$ Myr.

^c The suffixes “-se” and “-pb” indicate calculations that include stellar evolution and a population of primordial binaries (see Sec. 3.2) respectively.

Table 6. Best-fit parameters for the King surface mass-density profile at $t \approx 1$ Myr for computed post-gas-expulsion configurations. Here, the systems evolve in a background residual gas potential (see Secs. 2.2 & 3.2.1) to form a star cluster with near-spherical core-halo structure (the CH-type morphology, see Table 2) within $t < 1$ Myr followed by the expulsion of the residual gas at $\tau_d \approx 0.6$ Myr. The resulting cluster profiles agree well with the observed projected mass-density profile of HD97950 (*c.f.*, Table 4, Fig. 11). All the legends are the same as in Table 5.

Config. name	Short name	k	$r_c('')$	$r_t('')$	χ^2	$R_{\text{lim}}('')$
m1000r0.1R1.1N10	A-Ia	2.3 ± 0.1	9.5 ± 0.7	672.4 ± 712	0.9	45.0
		2.4 ± 0.2	9.0 ± 0.5	1242.6 ± 626	1.1	110.0
m1000r0.3R1.1N10	A-Ib	5.7 ± 0.6	5.8 ± 0.6	269.3 ± 180	2.4	40.0
		6.0 ± 0.7	5.1 ± 0.4	2110.7 ± 2574	2.6	110.0
m10-150r0.1R1.1N150	B-Ia	5.4 ± 0.5	6.5 ± 0.6	160.6 ± 44	2.6	50.0
		5.6 ± 0.6	5.5 ± 0.4	697.9 ± 284	3.1	110.0
m1000r0.3R1.1N10-pb	A-Ib-pb	4.2 ± 0.8	6.8 ± 0.8	934.1 ± 435	1.6	6.0 – 110.0
		2.6 ± 0.2	10.8 ± 1.0	174.5 ± 43	2.4	55.0

The quality of the King profile fit degrades moderately (see the χ^2 column) if the outer halos of the clusters are included ($R_{\text{lim}} \approx 110''$) when compared to that for only their inner regions ($40'' \lesssim R_{\text{lim}} \lesssim 60''$). In both cases, the fits are consistent with large values of r_t implying untruncated, monolithic cluster profiles as observed in HD97950 (see Table 4).



Figure 1. An image of NGC 3603 where the central star cluster is HD 97950 which we aim to reproduce, from model N-body calculations, in this study. This is a composite image obtained from the Hubble Space Telescope using the filters F128N (Paschen-beta), F164N ([Fe II]), F555W (V), F657N (H-alpha) and F673N ([S II]). The image is $\approx 180''$ (5 pc) wide. *Credit:* NASA, ESA, R. O'Connell (University of Virginia), F. Paresce (National Institute for Astrophysics, Bologna, Italy), E. Young (Universities Space Research Association/Ames Research Center), the WFC3 Science Oversight Committee, and the Hubble Heritage Team (STScI/AURA). This image is obtained from the online resource *hubblesite.org* (public domain).

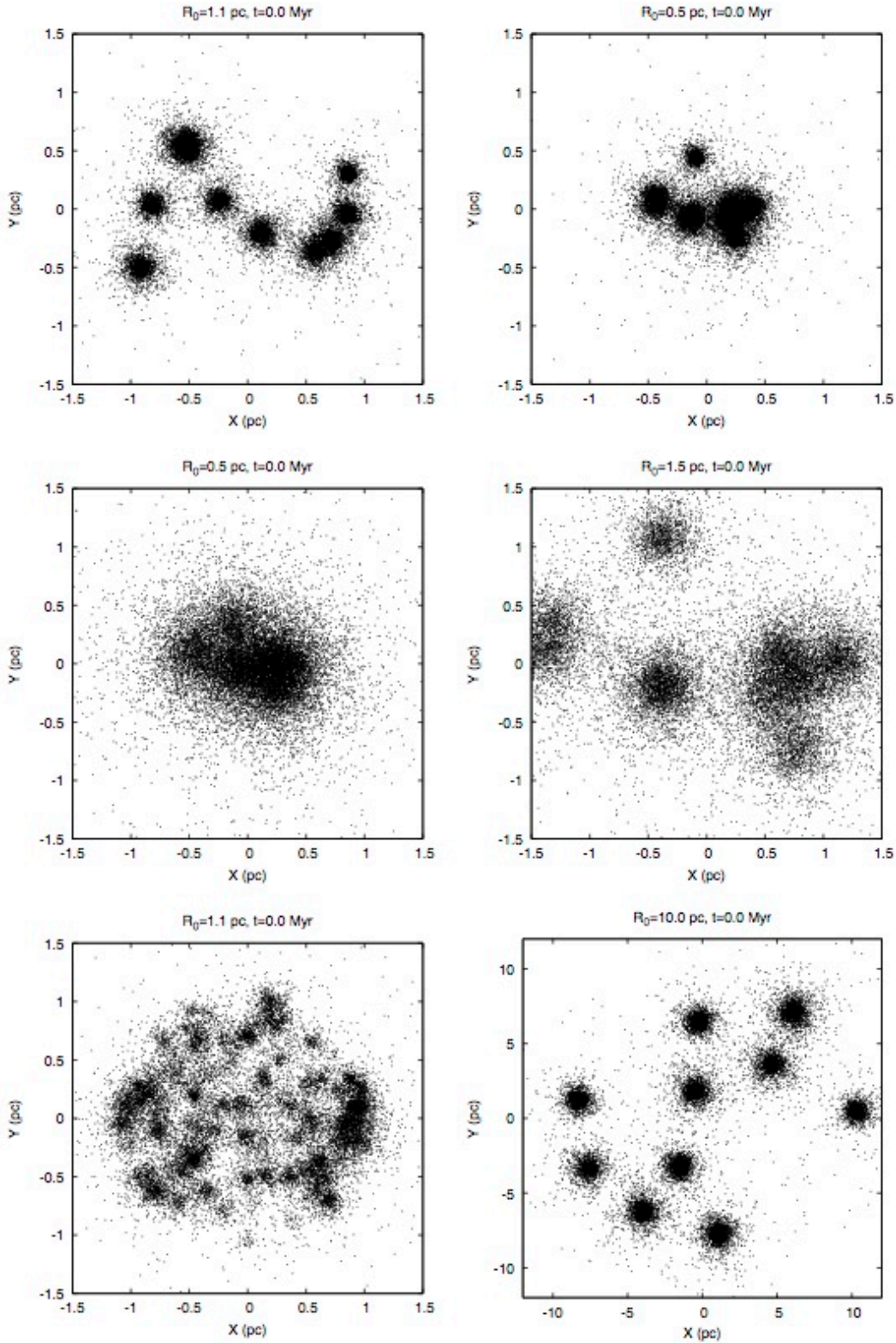


Figure 2. The primary varieties of the *initial* configurations that are evolved in this study, shown in projection. In this and all the subsequent figures, the panels are numbered left-to-right, top-to-bottom. In each case, a set of Plummer spheres (subclusters) are uniformly distributed over a spherical volume of radius R_0 , totalling a stellar mass of $M_* \approx 10000M_\odot$. Panels 1, 2, 3, 4 and 6 are examples of type A or “blobby” systems containing 10 subclusters of $m_{cl}(0) \approx 10^3 M_\odot$ each. With smaller R_0 , the subclusters overlap more with each other (*c.f.* , panels 1 & 2 with subcluster half mass radius $r_h(0) \approx 0.1$ pc and panels 3 & 4 with $r_h(0) \approx 0.3$ pc). This is also true for increasing $r_h(0)$ (*c.f.* , panels 1 & 4). Panel 5 is an example of type B or “grainy” initial configuration containing ≈ 150 subclusters of mass range $10M_\odot \lesssim m_{cl}(0) \lesssim 100M_\odot$. While panels 1-5 are examples of “compact” configurations, for which $R_0 \leq 2.5$ pc, panel 6, with $R_0 = 10$ pc, represents an “extended” configuration where the subclusters are much more distinct. See Sec. 2 for details of the initial setups. Tables 3 and 5 provide a complete list of initial systems computed here.

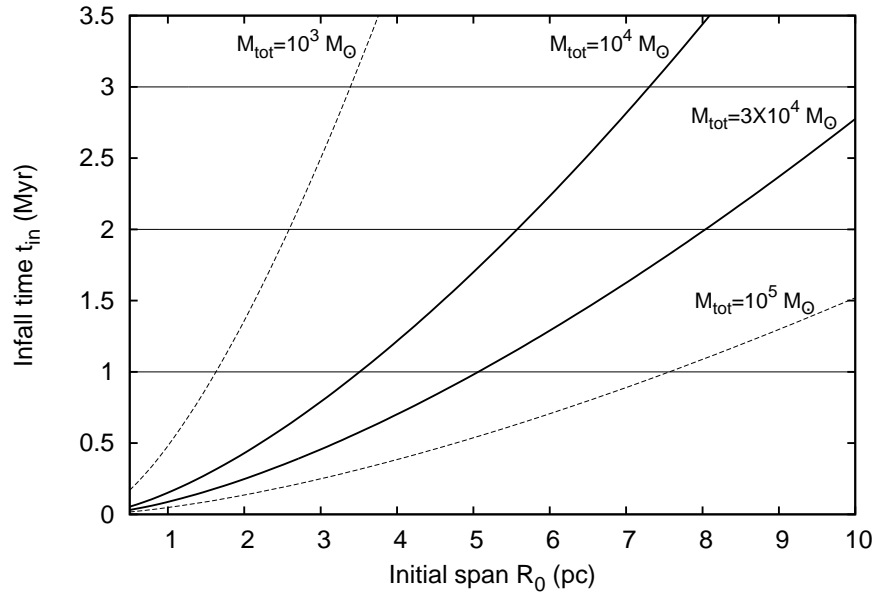


Figure 3. The infall time (or the time of first arrival at orbital pericenter; see Sec. 3.1) of the subclusters, t_{in} , as a function of the radius, R_0 , of the spherical volume over which they are initially distributed. The curves are according to Eqn. 2 for different systemic mass M_{tot} . For the present calculations, $M_{tot} = M_* = 10^4 M_\odot$ without a residual gas and $M_{tot} = 3M_* = 3 \times 10^4 M_\odot$ with the residual gas (see Sec. 2.2). These two curves are highlighted.

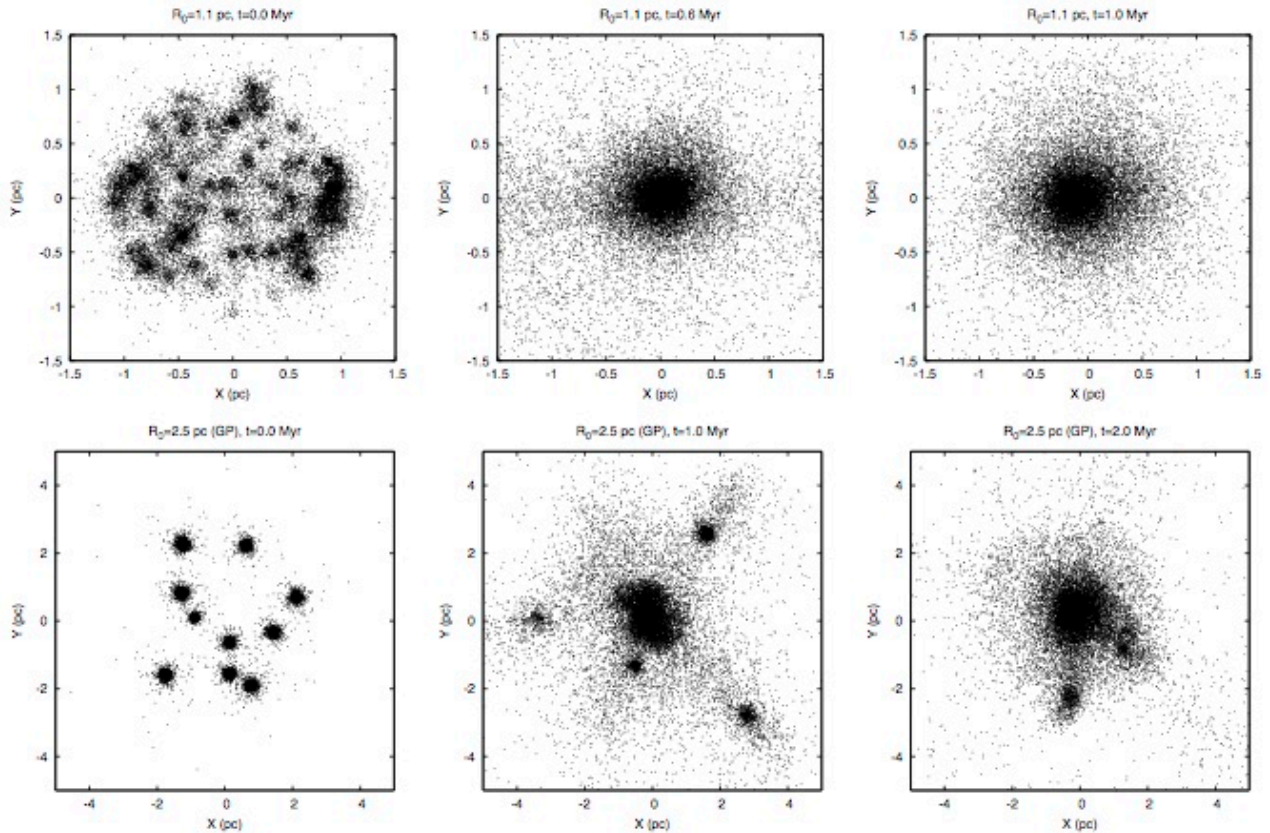


Figure 4. Examples of evolution of “compact” configurations, *i.e.*, configurations computed here which are initially distributed over spherical volumes of radii $R_0 \leq 2.5$ pc. These constitute all the initial systems abbreviated as *I* and *II* in Tables 3 and 5. Here, the evolutions of the systems B-Ia and (upper 3 panels) and A-IIa (lower 3 panels) are shown. “GP” indicates the presence of a gas potential (Sec. 2.2).

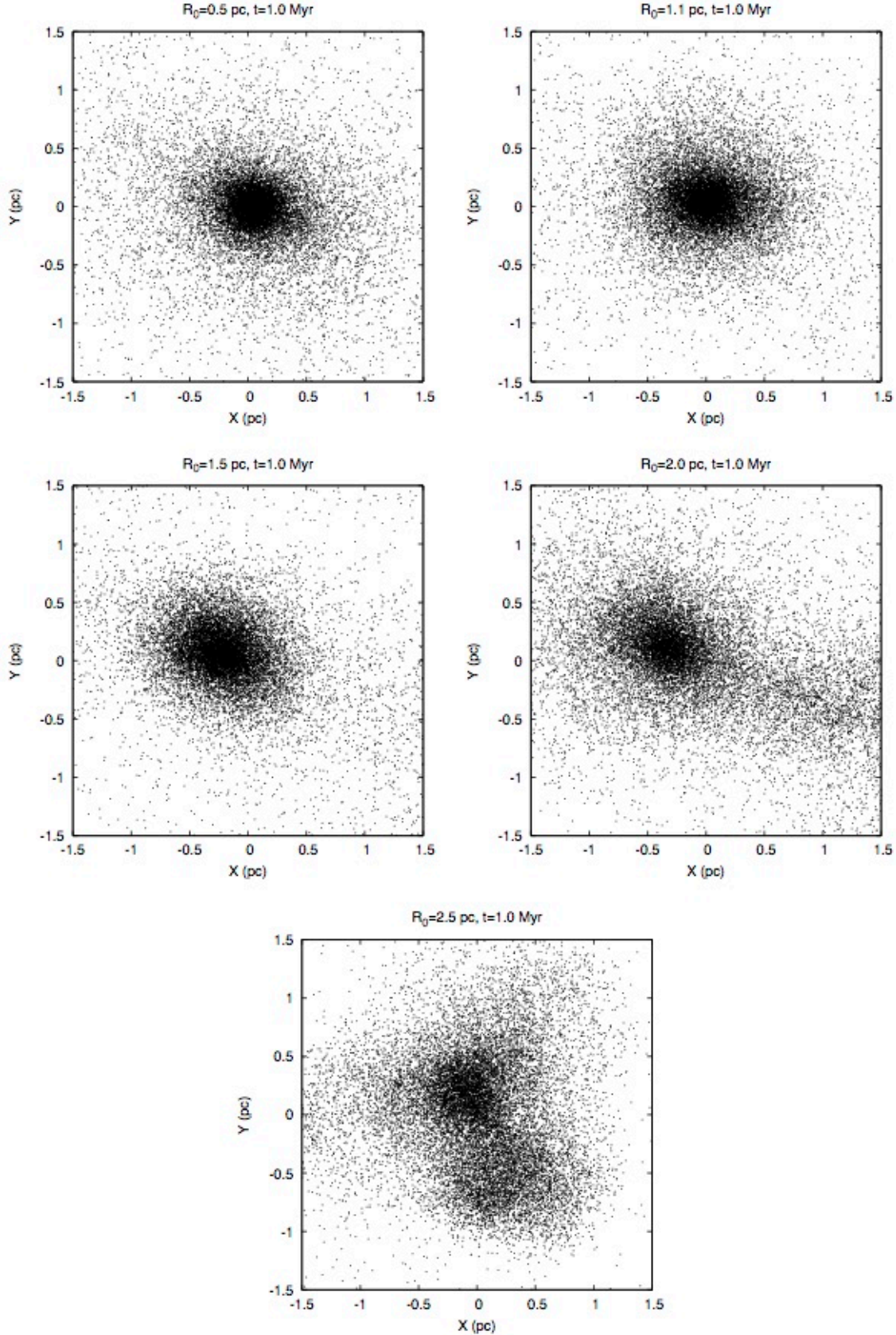


Figure 5. Configurations obtained at $t \approx 1$ Myr with increasing initial span R_0 for gasless “compact” Type-A systems with $r_h(0) = 0.3$ pc, namely, the systems A-0.5Ib, A-Ib, A-1.5Ib, A-2.0Ib and A-IIb (panels 1-5 respectively, numbered left-to-right, top-to-bottom; see Tables 3 and 5). With increasing R_0 , the system’s morphology at $t \approx 1$ Myr changes from being near-spherical core-halo (CH; panels 1,2), asymmetric core-halo (CHas; panels 3,4) to substructured (SUB; panel 5). For $R_0 \gtrsim 2$ pc (panels 4,5), the stellar system is still well in the process of merging at $t \approx 1$ Myr after the subclusters’ first pericenter crossings (*i.e.*, it is in the violent relaxation phase $t_{in} < t < t_{in} + t_{vr}$; see Sec. 3.1).

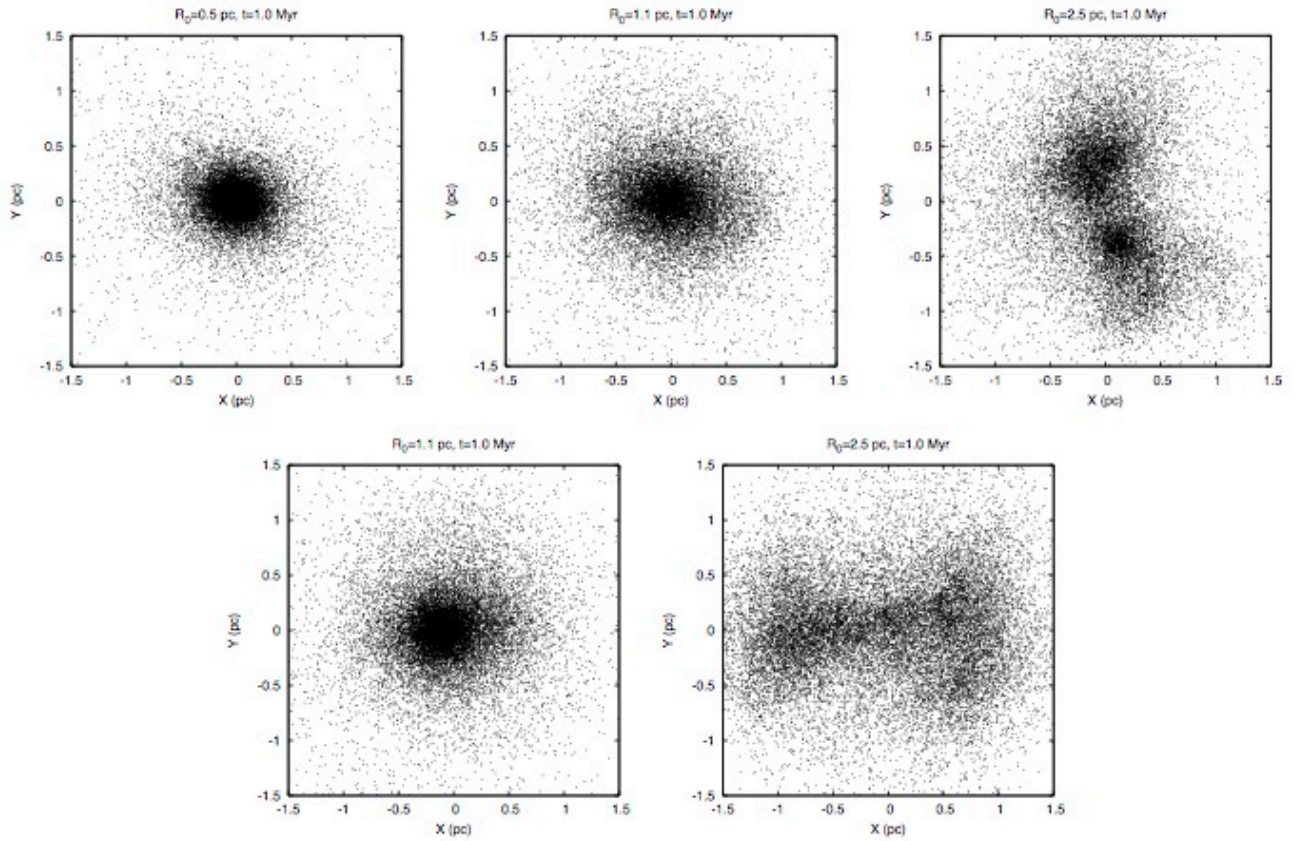


Figure 6. Configurations at $t \approx 1$ Myr with increasing initial span R_0 for gasless “compact” Type-A (upper three panels) and Type-B (lower two panels) systems with $r_h(0) = 0.1$ pc. These are the systems A-0.5Ia, A-Ia, A-IIa, B-Ia and B-IIa respectively (see Tables 3 and 5). As in Fig. 5, the configurations change through CH, CHas and SUB with increasing R_0 . For $R_0 = 2.5$ pc, the stellar system is still in the merging process at $t \approx 1$ Myr, likewise in Fig. 5.

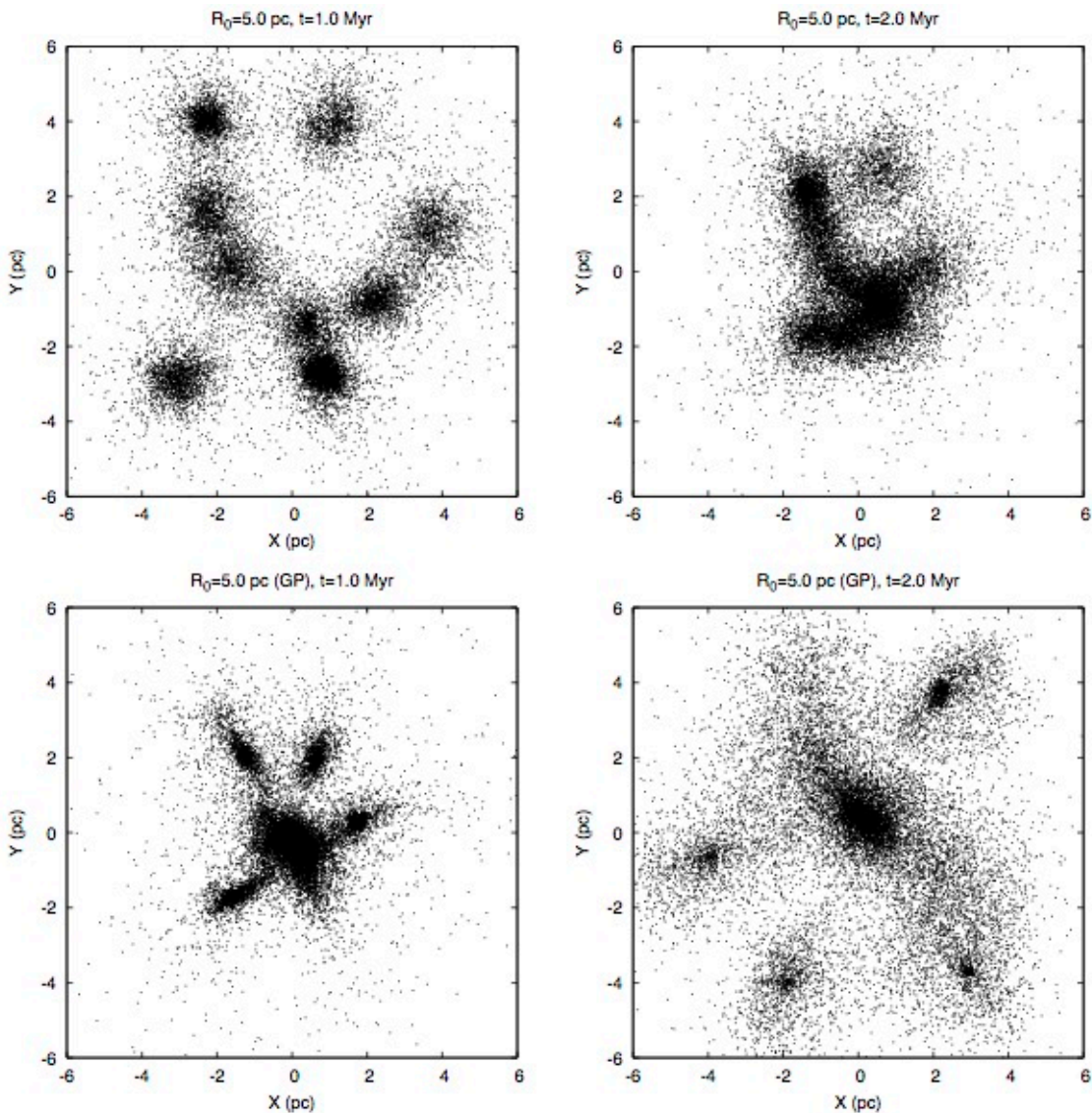


Figure 7. Evolution for the “extended” system A-IIId ($R_0 = 5$ pc; see Table 3). As expected, the infall of the subclusters proceeds much more slowly than that for the compact systems (*c.f.*, Figs. 4). The system is still highly substructured (SUB) at $t \approx 2.0$ Myr both in absence (panels 1,2, numbered left-to-right, top-to-bottom) and presence (panels 3,4) of a gas potential. In presence of the gas potential, the subclusters are close to the first arrival at their pericenters (*i.e.*, $t \approx t_{in}$; see Sec. 3.1) at $t \approx 1$ Myr (panel 3) while this takes $t \approx 2$ Myr without the gas (panel 2). This is consistent with Fig. 3. For the evolution with gas potential, the subclusters make their first passage through each other during 1 – 2 Myr which is why their configuration at 2 Myr (panel 4) is more extended than that in 1 Myr (panel 3). Note that the gas potential tidally elongates the subclusters significantly (also see Fig. 8).

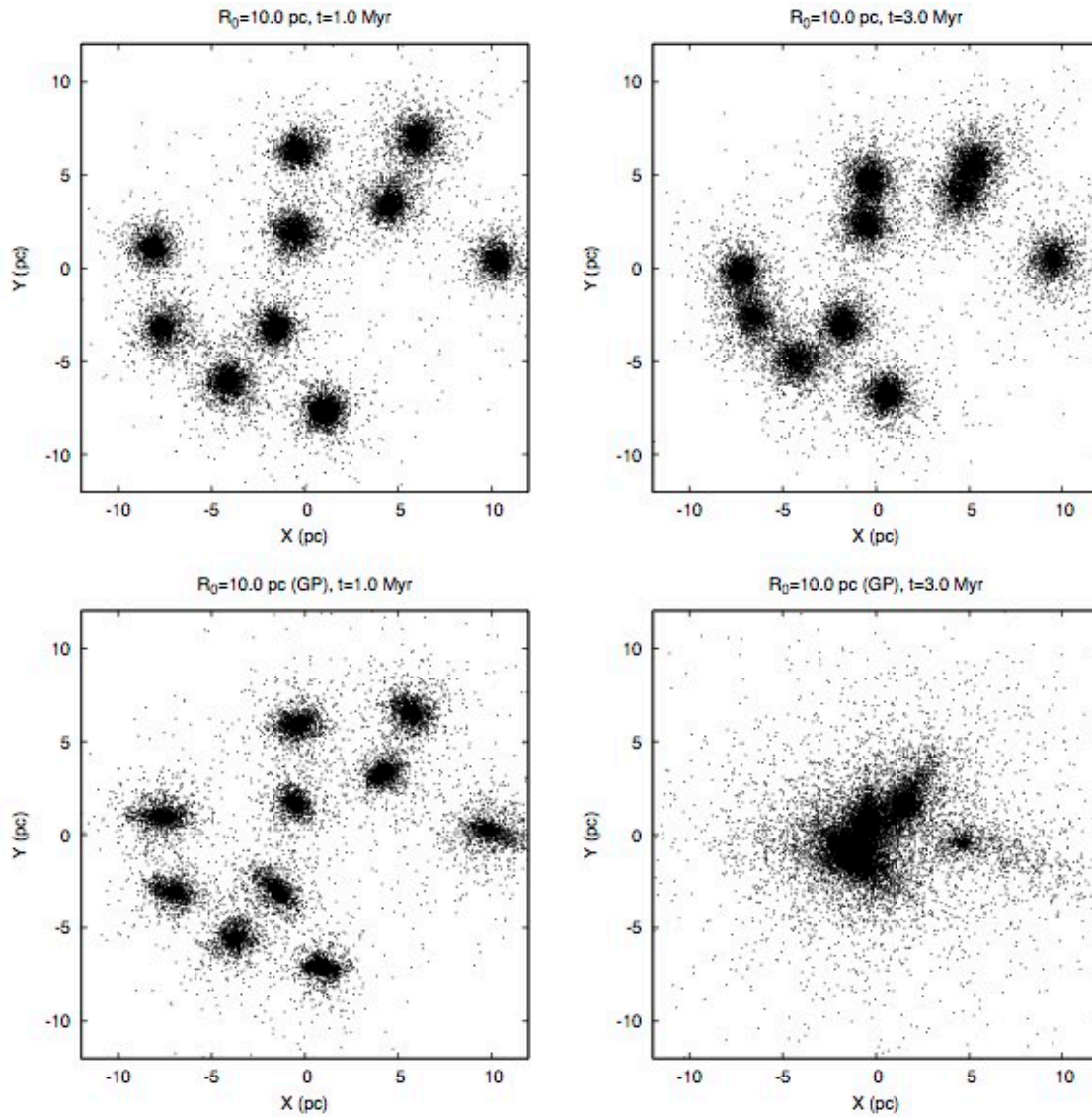


Figure 8. Evolution for the “extended” system A-IVd ($R_0 = 10.0$ pc; see Table 3) without (panels 1-2, numbered left-to-right, top-to-bottom) and with (panels 3-4) gas potential as in Fig. 7. In both cases, the system still remains highly substructured at $t \approx 3$ Myr. With the gas potential, the subclusters arrive at their pericenters for the first time at $t \approx 3$ Myr (panel 4) but are far from reaching there at that time without the gas (panel 2), being consistent with Fig. 3.

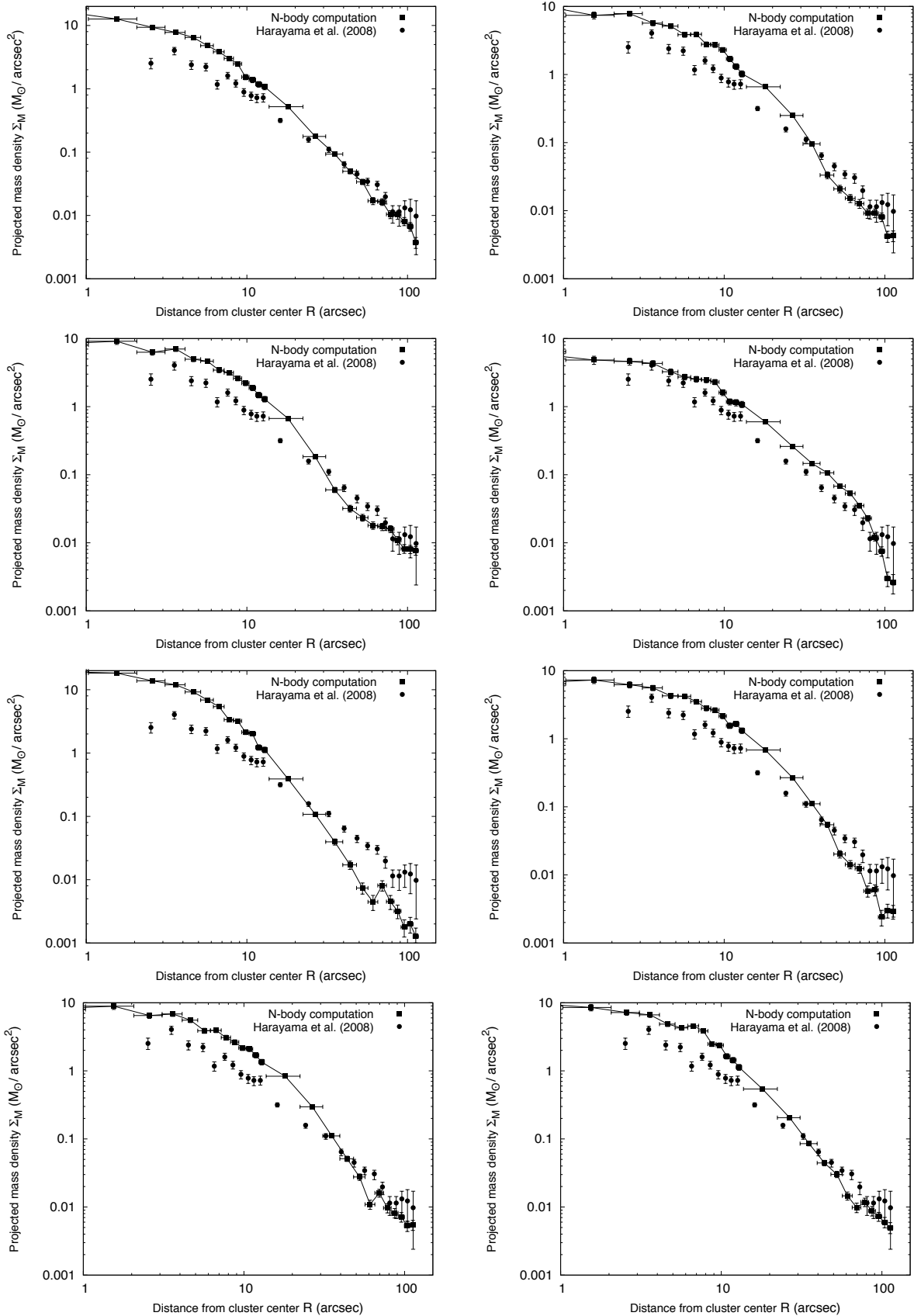


Figure 9. Surface mass-density profiles at $t \approx 1$ Myr for those computed configurations (filled squares connected with solid line) which evolve to form a star cluster with near-spherical core-halo structure (the CH-type morphology; see Table 2) within $t < 1$ Myr, in absence of a background gas potential. These systems are A-0.5Ib, A-Ib, A-1.5Ib, A-2.0Ib, A-0.5Ia, A-Ia, B-Ic and B-Ia (Table 5) as shown in panels 1-8 respectively (numbered left-to-right, top-to-bottom). All these computed profiles are significantly more compact and centrally overdense than the observed one for HD97950 (Harayama et al. 2008; filled circles). This is also evident from Tables 4 and 5. For HD97950 $1'' \approx 0.03$ pc.

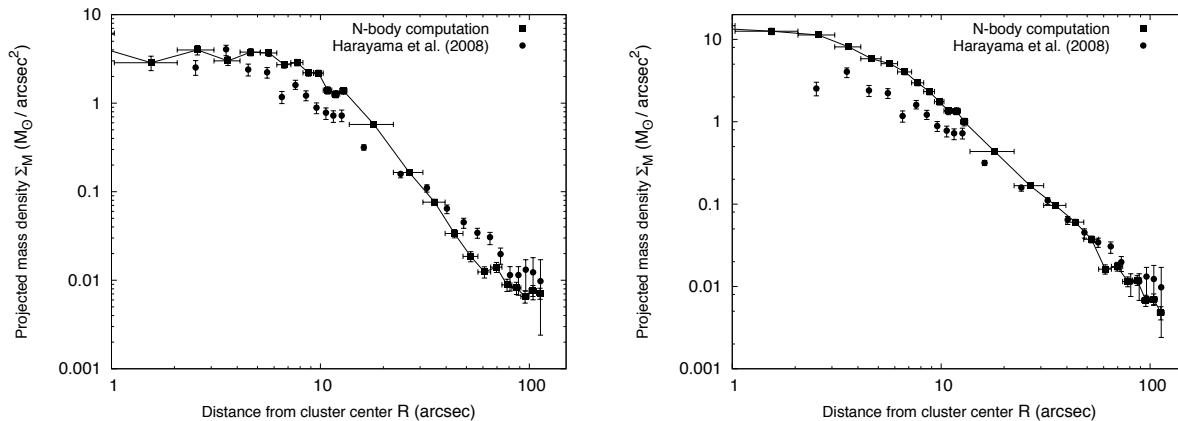


Figure 10. Similar as Fig. 9 but for a system containing primordial binaries (left, system A-Ib-pb) and a system including stellar evolution (right, system A-0.5Ib-se). Here, all legends are the same as in Fig. 9. Neither the dynamical heating effect due to primordial binaries nor the wind mass loss from the stars can prevent the merged structure from being substantially overdense and more compact compared to the observed one. This is also evident from Tables 4 and 5.

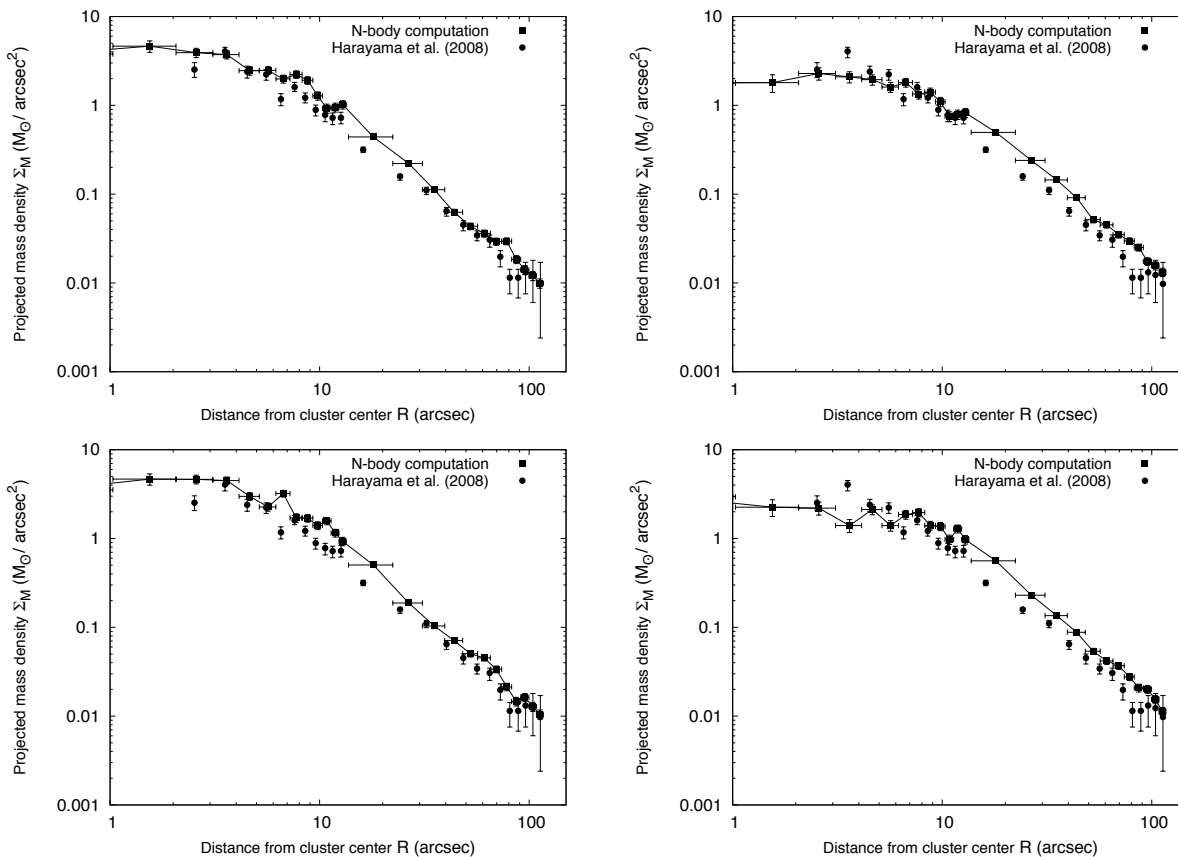


Figure 11. Surface mass-density profiles at $t \approx 1$ Myr for computed post-gas-expulsion configurations. Here, the systems evolve in a background residual gas potential (see Secs. 2.2 & 3.2.1) to form a star cluster with near-spherical core-halo structure (the CH-type morphology, see Table 1) within $t < 1$ Myr followed by residual gas dispersal at $\tau_d \approx 0.6$ Myr. The legends are the same as in Fig. 9. Panels 1-4 (numbered left-to-right, top-to-bottom) are for the configurations A-Ib, A-Ia, B-Ia and A-Ib-pb respectively (Table 6). All these profiles agree well with the observed one for HD97950 as is also evident from Tables 4 and 6.

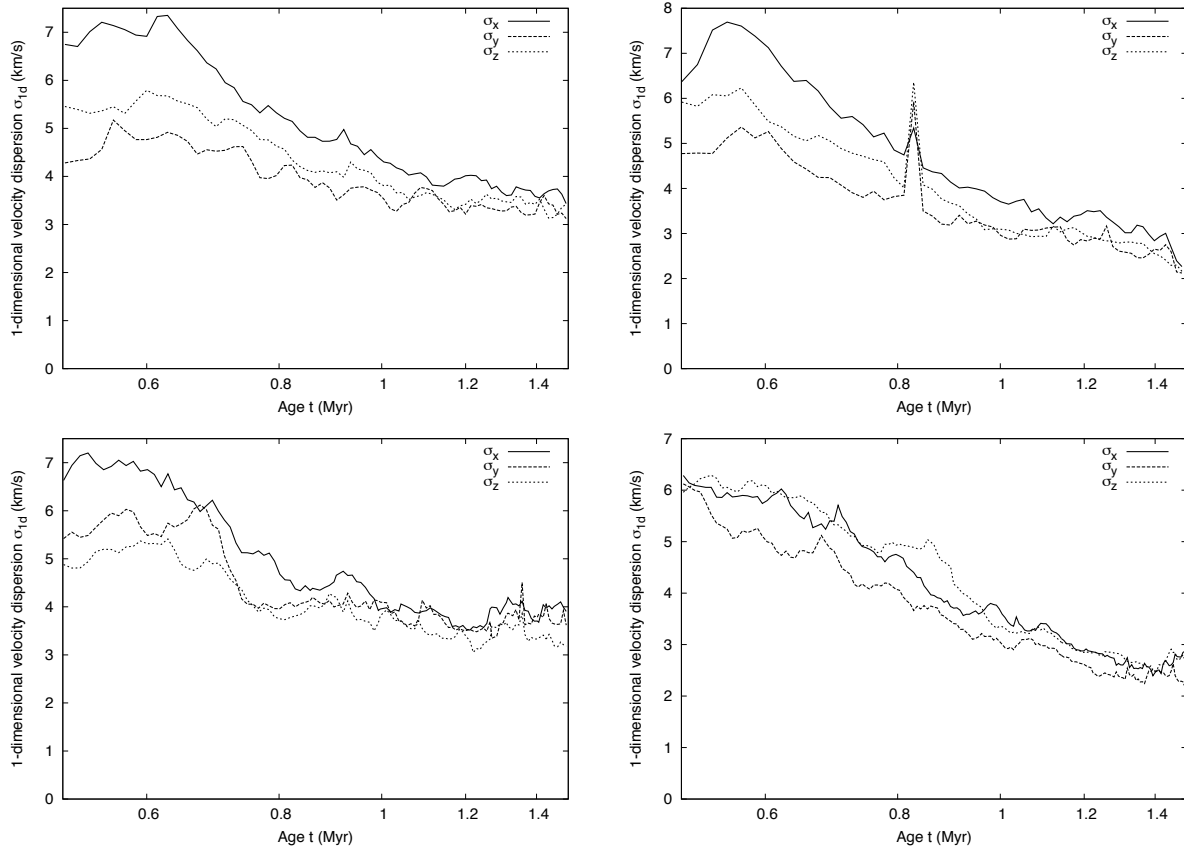


Figure 12. Evolution of 1-dimensional velocity dispersion σ_{1d} for the calculations corresponding to Fig. 11. The values of σ_{1d} are obtained over the stellar mass range $1.7M_{\odot} - 9.0M_{\odot}$ for the central $R \leq 0.5$ pc of each cluster as in Rochau et al. (2010).